AGU ADVANCING EARTH AND SPACE SCIENCE

Water Resources Research

RESEARCH ARTICLE
10.1029/2020WR028127

Special Section:
Advancing process representation in hydrologic models: Integrating new concepts, knowledge, and data

Interactions of Microtopography, Slope and Infiltration Cause Complex Rainfall-Runoff Behavior at the Hillslope Scale for Single Rainfall Events

Daniel Caviedes-Voullième[1,2,3,4], **Ebrahim Ahmadinia**[1], **and Christoph Hinz**[1]

[1]Chair for Hydrology - Brandenburg University of Technology Cottbus-Senftenberg, Cottbus, Germany, [2]Jülich Supercomputing Centre, SimLab Terrestrial Systems, Forschungszentrum Jülich, Jülich, Germany, [3]Centre for High Performance Scientific Computing in Terrestrial Systems - Geoverbund ABC-J, Jülich, Germany, [4]IBG3: Agrosphere - Forschungszentrum Jülich, Jülich, Germany

Key Points:

- Microtopography plays a relevant role in rainfall-runoff-infiltration partitioning
- Different slopes and microtopographies result in a set of hydrodynamic regimes
- The hydrodynamic regimes can be related to hydrological regimes

Supporting Information:

Supporting Information may be found in the online version of this article.

Correspondence to:

D. Caviedes-Voullième,
d.caviedes.voullieme@fz-juelich.de

Citation:

Caviedes-Voullième, D., Ahmadinia, E., & Hinz, C. (2021). Interactions of microtopography, slope and infiltration cause complex rainfall-runoff behavior at the hillslope scale for single rainfall events. *Water Resources Research*, *57*, e2020WR028127. https://doi.org/10.1029/2020WR028127

Received 9 SEP 2020
Accepted 4 JUN 2021

Abstract Microtopography (MT) can govern runoff dynamics as a net result of local heterogeneities in the flow paths and ponding. This in turn controls the development of the surface water layer that connects and flows downslope. It is therefore important to understand which microtopographic features affect runoff generation dynamics and its macroscopic—hillslope scale—hydrological signatures (e.g., hydrographs, runoff and infiltration volumes). In this study, we numerically solve 2D overland flow from a single rain pulse on 1,460 idealized hillslopes with different slopes and sinusoidal microtopographies and different infiltration capacities. We assess hydrodynamic distributions, hydrographs and hydrological indices to assess the effects of MT and infiltration on the (local) hydrodynamic and (larger scale) hydrologic responses in terms of surface runoff regimes. The results show that MT enhances infiltration and that infiltration and runoff depend in a strong non-linear way on slope and the properties of MT. Three regimes of influence of MT were identified: one in which MT plays a negligible role but there is a high sensitivity to the infiltration capacity curve, a second regime in which hydrological partitioning is highly sensitive to MT and the infiltration capacity curve, and a third regime in which MT increases infiltration, but the response is insensitive to particular features, and more affected by the average slopes. The regimes are the product of the interplay between small (MT) and large scale (slope) properties. Furthermore, the results suggest that hydrological signatures can be interpreted and explained by the spatiotemporal variation of surface connectivity.

1. Introduction

Runoff generation and the consequent overland flow are an observable result of multiple interactions between gravity-driven flow over complex surfaces, ponding at local depression, friction forces, and infiltration. These hydrodynamic processes occur at different spatiotemporal scales, often rather small (below the meter scale), but result in fluxes which aggregate along the landscape and manifest as observable behaviors at hillslope and catchments scales. Through this *flux rescaling* process, the small and local scales fluxes have a net effect on hillslope and catchment hydrological response. This complex multiscale process is still poorly understood (Ries et al., 2017).

Microtopography (MT)—also referred to as surface roughness or micro-relief (Smith, 2014)—affects the onset of runoff (Dunne et al., 1991; Khosh Bin Ghomash et al., 2019; Thomas et al., 2017), runoff connectivity (Thomas et al., 2017), flow and transport pathways (Helming et al., 1998), drainage networks (Luo et al., 2017), and directions of subsurface flow (Sande & Chu, 2012; Van der Ploeg et al., 2012). MT can therefore affect other fluxes across the landscape, for example, sediment (Luo et al., 2020; Turunen et al., 2020), pollutant and nutrient fluxes (Chu, Nelis et al., 2013; Frei et al., 2012; Thomas et al., 2017). These mediate the impact of MT on long term ecohydrological and geomorphological processes (Grieve et al., 2016; Harman et al., 2014), vegetation establishment (McGrath et al., 2012), acclimation (Le & Kumar, 2017), and soil formation (Wainwright & Bracken, 2011). Although a precise definition of MT is elusive (Smith, 2014), it is usually defined as the very small scale features, with vertical dimensions akin to water depth and horizontal dimensions around the decimeter scale (which is orders of magnitude below the hillslope scale), and encompasses from surface roughness (around the centimeter scale) (Darboux et al., 2002) to rills and gullies (centimeters to decimeters) (Dunne et al., 1991; Thomas et al., 2017).

Rainfall over MT triggers complex and transient hydrodynamics, understood as the water depth and velocity spatial distributions or fields. This response has prompted a set of flow regime classifications based on inundation of the MT and hydrological flow regimes, ranging from local to sheet flow (Darboux & Huang, 2005; Thompson et al., 2010). The sequence and combination of the hydrodynamic regimes can strongly affect the partitioning of rainfall into runoff and infiltration, hereafter referred to as the *hydrological response*. In short, there is a complex spatiotemporal dependence of both the hydrodynamic and hydrological response on MT throughout a rainfall-runoff event. This dependence is not well captured by simple statistical models of MT that are typically used to transfer measured MT into simpler structural proxies (Smith, 2014), as they neglect key aspects such as surface detention and lag times (Antoine et al., 2011), MT anisotropy (García-Serrana et al., 2018; Viero & Valipour, 2017) and spatial variation (Kamphorst et al., 2005), interactions with infiltration and storm properties (Fernández-Pato et al., 2016; Thompson et al., 2010; Yang & Chu, 2013). Most importantly, such proxies are limited to represent mostly local, patch-scale areas, thus not addressing multiscale interactions at the larger hillslope and catchment scales (Antoine et al., 2009; Descroix et al., 2007). An additional level of complexity arises from the interactions between surface flow and infiltration. Infiltration models approximate only certain parts of the infiltration process well (Mishra et al., 2003), which together with MT can make calibration of models difficult (Fernández-Pato et al., 2016; Langhans et al., 2011). There are few systematic assessments of how simplifying assumptions of infiltration models interact with MT. For example, Rossi and Ares (2012) performed plot scale experiments and found that depressions have an influence of runoff/infiltration beyond that of a passive storage. Other studies have shown that MT has complex interactions with runoff (Fernández-Pato et al., 2016), infiltration (Thompson et al., 2010) and complex surface-subsurface interactions and implications on biogeochemistry (Frei et al., 2010, 2012). This gap prompts the need to analyze how these components interact within a modeling context (Yang & Chu, 2013).

The complex runoff-generating interactions generate complex 2D hydrodynamics, that determine dynamic flow connectivity (Antoine et al., 2009, 2011; Appels et al., 2011; Le & Kumar, 2014; Peñuela et al., 2016; Yang & Chu, 2013) and emergent behaviors such as threshold responses and leakiness (Cammeraat, 2004) and a reduction in runoff ratios with hillslope size (Cammeraat, 2002). Several studies have investigated the effects of MT on hydrological partitioning (Chu, Yang et al., 2013; Dunne et al., 1991; Frei & Fleckenstein, 2014; Frei et al., 2010; Peñuela et al., 2016; Thompson et al., 2010; Turunen et al., 2020; Van der Ploeg et al., 2012; Zhao & Wu, 2015), however, mostly without systematically exploring different surface properties and slopes. Additionally, the spatiotemporal features of the flow due to MT affect travel times (Zhao & Wu, 2015), pathways (Frei et al., 2012; Voter & Loheide, 2018) and may lead to biogeochemical hotspots (Frei et al., 2012; McClain et al., 2003).

Investigating the interdependence of (large scale) slope and (small scale) MT is constrained in laboratory and plot scales experiments, and unfeasible for hillslope experiments, since the hydrodynamics are hard to measure, and it is difficult to span across scales. An alternative approach is to perform numerical simulations spanning a large parameter space that reflects realistic combinations of slope, MT, time dependent infiltration, etc., and to study the relation between small scale variability and large(r) scale responses and hydrological signatures—that is, indices which represent hydrological outcome of one or more processes (e.g., Addor et al., 2018; McMillan et al., 2017). Of particular interest are systematic studies focusing on simple idealized, sinusoidal MT perpendicular (Dunne et al., 1991) or parallel (Thompson et al., 2010) to the flow. These studies have found that MT results in an *infiltration enhancement* (Darboux & Huang, 2005; Thompson et al., 2010) in comparison to smooth surfaces without MT. That is, MT increases the infiltration volume and decreases the runoff volume. Although simple idealized surfaces may not be very realistic, their use facilitates characterizing the MT by simple indices (e.g., amplitude and wavelength), in contrast to more realistic and complex surfaces (Smith, 2014). Consequently, this facilitates the comparability and interpretability and allows investigation of the interactions between features and processes without exploring a very large parameter space. Despite being a rather parsimonious model, sinusoidal MT still allows for all processes that are relevant for connectivity: ponding, flow-channel formation, puddle-to-puddle dynamics and sheet flow. Parsimonious representations of spatial complexity have been shown to be effective in generating appropriate runoff dynamics (Müller et al., 2007). Moreover, as eloquently stated by Thompson et al. (2010), the behavior of the idealized set up must be captured by any general theory that is also valid for realistic surfaces, making it a benchmark case, and a first step which allows progressive introduction of

more complexity (Van der Ploeg et al., 2012). The idea of simplified and periodic MT has recently been explored in laboratory scale experiments (Hu et al., 2020). Additionally, some systems do show similar structures, such as Gilgai (Khitrov, 2016; Kishné et al., 2014) and forest pit-mound MT (Valtera & Schaetzl, 2017) for which hydrological insights resulting from idealized surfaces may be particularly relevant.

This work aims to contribute to a better understanding of the conditions under which MT affects surface runoff and hydrodynamics and thus on hydrological regimes. We perform an analysis of rainfall-runoff-infiltration simulation on hillslopes with sinusoidal MT in 2D. Specifically, the goals of this study are to (a) systematically assess the effects of MT on rainfall-runoff-infiltration partitioning at the onset of runoff, by comparing it to the partitioning for a reference smooth surface. (b) Identify relationships between the spatiotemporal hydrodynamics (depths, inundation distributions) resulting from rainfall and hillslope scale hydrograph characteristics, and how such relationships depend on MT. (c) Perform a first assessment of the effect of the temporal variation in infiltration capacity and MT on the partitioning of rainfall into runoff and infiltration dynamics. (d) Evaluate how simple microtopographic indices (depression storage, and the ratio of wavelength to amplitude), which are structural characteristics, can contribute to comparatively assess hydrological responses of different systems, representations and models.

To reach these goals, we performed a large set of simulations using a physically based 2D surface water model with both a constant infiltration capacity (CIC) model and a non-constant infiltration capacity model (NIC). We assess systematically the effects of the slope, amplitude and wavelength of the surfaces on the hydrological partitioning, hydrographs, and spatiotemporal water depth distributions. We group our findings into distinctive flow regimes and hydrograph shapes and characteristics to show the multiscale nature of the response.

This study is inspired on the previous works by Dunne et al. (1991), who studies 1D MT perpendicular to the slope, and Thompson et al. (2010) who studied the effects of 1D MT parallel to the slope. The 2D setup in our study extends these efforts. The extensive study by Thompson et al. (2010) included many interacting processes and explored a wide parameters space (various amplitudes and wavelengths, rainfall intensities and duration, hydraulic conductivities). However, it is limited by its 1D nature, rendering it incapable of describing the hydrodynamic complexity and connectivity over 2D MT and the full spectrum of flow regimes. In contrast, we focus on the interactions of MT, slope and infiltration models. Furthermore, we use a large range of slopes instead of the two slopes (0.035, 0.17) studied by Thompson et al. (2010). This allows us to explore an extended set of combinations of large scale and micro scale topographic features. The 2D model further allows us to explore the onset of runoff connectivity. We also consider and compare constant and transient infiltration models, to explore the possible implications of the transient nature of the infiltration process. Contrary to Thompson et al. (2010) we do not require an estimation of time to ponding, as ponding emerges naturally in the computational model. Additionally, our analysis seeks to link hydrologic partitioning, hydrograph shapes and runoff connectivity to MT, while also relating these to the flow regimes originally proposed (but not simulated) by Thompson et al. (2010).

2. Materials and Methods

2.1. Mathematical and Numerical Model

Simulating the partitioning of rainfall into infiltration and runoff requires to solve physically based equations in a 2D domain, that is discretized fine enough to explicitly represent MT, so that it is possible to assess how local water fluxes add up and re-scaled into larger flows. Herein, the Zero-Inertia (ZI) approximation to the shallow-water equations is used for surface flow simulation. This equation is obtained by neglecting all acceleration terms in the momentum equation (Caviedes-Voullième et al., 2018) which results in a steady momentum equation containing hydrostatic, bed and friction terms (here expressed in terms of Manning's equation). This approximation has been shown to be applicable for the type of rainfall-runoff problems of interest here (Caviedes-Voullième, Fernández-Pato et al., 2020). The ZI equation is

$$\frac{\partial h}{\partial t} + \nabla\left(\frac{h^{5/3}}{n\sqrt{|\mathbf{Z}|}}\mathbf{Z}\right) = r - i \tag{1}$$

where h $[L]$ is depth, z $[L]$ is bed elevation, $\mathbf{Z} = -\nabla\left(h + z\right)$ is the surface gradient, n $[TL^{-1/3}]$ is Manning's roughness coefficient, r $[LT^{-1}]$ is rainfall intensity and $i\left[LT^{-1}\right]$ is the infiltration rate.

By invoking the Finite Volume method, discretizing all quantities into piece-wise constant approximations, and explicit integration with a Forward Euler scheme, the discrete form of the ZI is obtained (Caviedes-Voullième, Fernández-Pato et al., 2020; Caviedes-Voullième et al., 2018).

$$h_j^{n+1} = h_j^n + \Delta t(r - i)_j^n - \frac{\Delta t}{A_j}\sum_{\omega=1}^{N_\omega}\frac{\left(h_\omega^n\right)^{5/3}}{n_\omega\sqrt{\left\|\mathbf{Z}_\omega^n\right\|}}\mathbf{Z}_\omega^n \cdot \mathbf{n}_\omega L_\omega \tag{2}$$

where j represents a computational cell with area A and N_ω edges. $\mathbf{n}_\omega$ is the outer-pointing vector normal to edge ω, which has a length L_ω. Superindices n and $n+1$ represent current and future times respectively. The gradient across an edge $\mathbf{Z}_\omega$ is defined as

$$\mathbf{Z}_\omega \cdot \mathbf{n}_\omega = \frac{h_k + z_k - h_j - z_j}{d_\omega} \tag{3}$$

where k is the neighbor cell to j across edge ω, with d_ω the distance between cell centers perpendicular to edge ω. Note that $\mathbf{Z}_\omega$ is well defined at the edge, but h_ω is not, and must be estimated to cope with its bi-valuated nature at such edge. Here, we take an upwinded approach (Caviedes-Voullième, Fernández-Pato et al., 2020).

2.2. Study Case Setup

The computational domain is a rectangle 8 × 3 m (inspired by Tatard et al., 2008), with a slope parallel to the x axis. All boundaries were set as closed (no flow) boundaries, except at $x = 8$ m, where a free outfall boundary was set. A 2D sinusoidal MT was superimposed on the sloping plane, with amplitude a and wavelength λ,

$$z(x, y) = a\sin\left(\frac{2\pi}{\lambda}x\right)\sin\left(\frac{2\pi}{\lambda}y\right) + sx + z_0 \tag{4}$$

where z is surface elevation $[L]$, x, y are the horizontal coordinates $[L]$, a is wave amplitude $[L]$, λ is wavelength $[L]$, s is slope $[L/L]$ in the x-direction, and z_0 is a reference datum $[L]$, which was constant as $z_0 = 1$.

The study systematically investigated 20 different slopes $s \in [0, 10]\%$, nine amplitudes $a \in [1, 9]$ cm and eight wavelengths $\lambda \in [0.15, 2.0]$ m (see Table A1 in Supporting Information for the complete set). All combinations of the three parameters were used, resulting in 1,440 surfaces. Additionally, 20 reference smooth plane surfaces, one for each slope ($a = 0$), were constructed. The mesh resolution was selected for each case based on the wavelength, so that resolution is at least $\delta x \leq \lambda/9$ (resulting in $0.0167 \leq \delta x \leq 0.09$ m for the range of wavelengths). This ensures that the shape of the sinusoidal wave is properly captured, while allowing for a minimal cell numbers and reasonable computational times.

Rainfall consisted of a single pulse of constant intensity of 7.5 mm h^{-1}, and duration of 1,800s (30 min), which represents a moderate rainfall event in a Mediterranean climate (Llasat, 2001), and was chosen because smaller events are unlikely to result in runoff, and very intense events will predominantly result in fast runoff and sheet flow. The simulation duration was set to 8,000 s to ensure that runoff ended before the end of the simulation. Manning's roughness coefficient was set to $n = 0.055$ $m^{-1/3}s$ for all cases, following the largest values used by Thompson et al. (2010). Infiltration is modeled in two ways: (i) CIC $f(t) = 3.6$ mm $h^{-1} = 10^{-6}$ mm s^{-1} (reference value used by Thompson et al,. 2010), and (ii) time-varying, NIC modeled with Horton's equation (Horton, 1933)

$$f(t) = f_c + \left(f_0 - f_c\right)e^{-kt} \tag{5}$$

where $f_c = 0.546$ mm h^{-1} is the asymptotic infiltration capacity, $f_0 = 2.184$ mm h^{-1} the initial infiltration capacity and $\kappa = 1\text{h}^{-1}$, which are representative for a loam or loamy clay (Akan, 1992). These parameters were selected so that the total infiltration volume by the end of the simulation time would be equivalent to that of constant infiltration (see Supporting Information for details). This in turn means that the (integral) average infiltration rate for both setups is comparable. Although it is recognized that alternative infiltration capacity models may be physically more meaningful (Mishra et al., 2003), for the purposes of this work Horton's model (Equation 5) is sufficient, as it generates a NIC that is easily parameterizable, in particular since we do not intend to represent any particular soil. Altogether, the computational experiment required 2,920 simulations. Simulations were run in a parallel setup of 20 × CPU i7-6950X @ 3.00GHz.

2.3. Indicators and Signatures

The simulations provide spatiotemporal patterns of hydrodynamic (water depth) and hydrological variables (infiltration rate, accumulated infiltration). The simulated hydrographs are used as a macroscopic signature of overland flow. These results allow for qualitative analysis of the overall response (large scale indicators). The depth distributions allow assessment of local flow features and assessment of the relevance of spatial variations of MT (Antoine et al., 2009) and flow networks (Roche et al., 2007) that affect flow regimes and hydrographs. Moreover, both the hydrodynamic distributions and the hydrographs can be related to different stages and flow regimes (Chu, Yang et al., 2013; Darboux & Huang, 2005; Roche et al., 2007; Thompson et al., 2010). Herein, we attempt to relate the connectivity of the overland flow and the outflow hydrographs to the runoff regime classification proposed by Thompson et al. (2010) that is based on the inundation of the surface, that is , local, channel, mixed and sheet flows.

We define additional indicators to quantitatively capture (macroscopic) hillslope responses for sensitivity analyses. These indicators allow us to summarize the combined effects of MT and infiltration on hydrologic partitioning. We first define the *infiltration enhancement ratio* $\tilde{I}$ following (Thompson et al., 2010),

$$\tilde{I} = \frac{I(s,a,\lambda)}{I_0(s)} \tag{6}$$

where $I_0(s)$ is the total infiltration volume (at the end of the simulation) for a smooth plane with slope s and $I(s, a, \lambda)$ is the total infiltration volume (at the end of the simulation) for a surface with slope s and with MT of amplitude a and wavelength λ. $\tilde{I}$ represents the factor by which MT enhances infiltration on a surface of slope s, and is expected to be $\tilde{I} \geq 1$.

In order to assess the effect of CIC versus NIC, we introduce $\tilde{I}_{cn}$, the ratio of $\tilde{I}_{cic}$ to $\tilde{I}_{nic}$ (infiltration enhancements for CIC and NIC respectively). The ratio describes how much infiltration capacity can modulate the effects of MT on hydrological partitioning. In addition, we also introduce I_{cn}, the ratio of I_{cic} to I_{nic} (infiltration volumes CIC and NIC respectively) to assess the effects of infiltration capacity on the overall water balance for the same surface.

$$\tilde{I}_{cn} = \frac{\tilde{I}_{nic}}{\tilde{I}_{cic}} \qquad I_{cn} = \frac{I_{nic}}{I_{cic}} \tag{7}$$

We also define the local accumulated fraction of infiltration F_i^* in a cell as

$$F_i^* = 100 \cdot F_i \left(\sum_j^N F_j \right)^{-1} \tag{8}$$

where N is the number of cells in the domain.

These infiltration indicators, the water depth distributions and hydrographs and the regimes identified from them, can be related to indicators that characterize the MT itself. Many such proxy MT indicators (or statistical representations) exist (Smith, 2014). These are all statistical indicators, and mostly focus on local, patch-scale areas and thus do not clearly address the interaction of these small scales with the larger hillslope scale and the resulting hydrological behavior (Descroix et al., 2007). In addition, they are sometimes incapable of

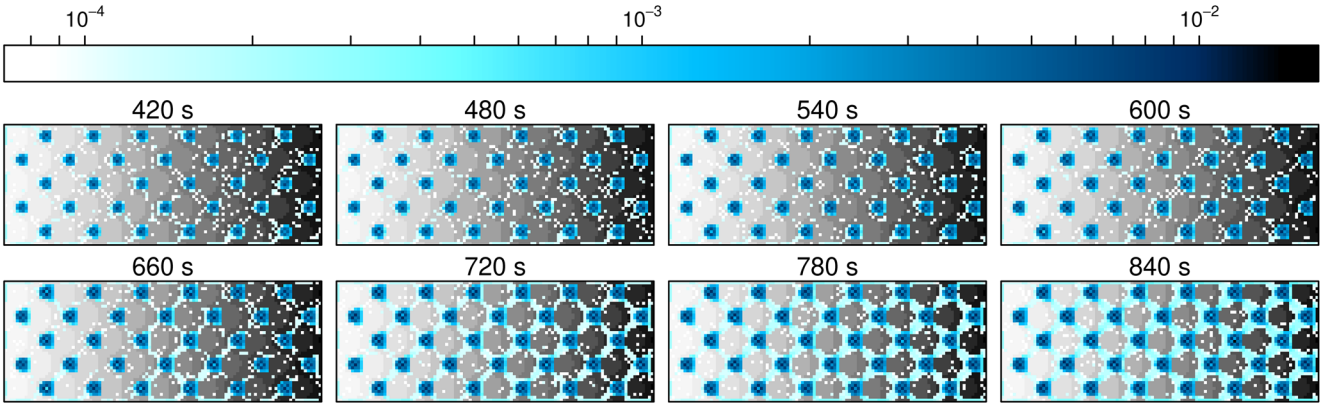

Figure 1. Transient water depth [m] during the onset of runoff for the surface with $s = 0.05$, $\lambda = 1.2071$ m and $a = 0.02$ m, and constant infiltration capacity. Gray shades illustrate topography (darker is lower), blue colors represent water depth. Water depths lower than 0.1 mm are not shown. The surfaces slope to the right. Rainfall duration is 1,800 s.

distinguishing MT with different hydrological response—for example, variograms (Darboux et al., 2002)—or are unable to represent spatial distributions—for example, random roughness (Kamphorst et al., 2005)—which make them poor indicators for hydrological dynamics (Antoine et al., 2009).

The first index related to MT is derived from maximum depression storage D [L^3], herein depression storage for brevity. This is a well-known and frequently used indicator (Hansen et al., 1999; Onstad, 1984; Turunen et al., 2020) that is a static, structural property of the surface. It is also easy to measure or estimate, and its mathematical representation is simple, especially in comparison to alternative indicators such as variograms (Darboux et al., 2002), fractals (García-Serrana et al., 2018) or tortuosity (Zhao & Liu, 2010). We define $\tilde{D}$ as the ratio of depression storage to the total rainfall volume R [L^3],

$$\tilde{D} = \frac{D}{R} \tag{9}$$

That is, under impervious conditions, runoff occurs when $\tilde{D} \geq 1$. We highlight that this normalization allows some level of generalization despite the single rainfall pulse used here instead of a range of rainfall properties.

The second index is the MT ratio $\tilde{M}$

$$\tilde{M} = \frac{\lambda}{a} \tag{10}$$

where $\tilde{M} \to \infty$ for smoother surfaces and $\tilde{M} \to 0$ for very rough surfaces. This indicator falls into the *extreme characteristics* and *feature spacing* parameters for parameterizing surface roughness as identified by Smith (2014). It is important to highlight that $\tilde{M}$ is strictly a property of the MT, as it only depends on wavelength and amplitude—that is, it is a single-scale property—whereas depression storage and therefore $\tilde{D}$ are multiscale properties of the surface, as they are functions of the local topographic slope and of the size of the hillslope itself (Darboux et al., 2002; Hansen et al., 1999; Onstad, 1984; Peñuela et al., 2015; Smith, 2014). Both indices are of interest, because it has been recognized that the scale dependencies are not trivial (Darboux et al., 2002; Smith, 2014).

3. Results

3.1. Spatiotemporal Distributions

The transient water depth distributions presented in Figure 1 for a selected case shows the runoff generation during the early stages of the event (an additional transient case is shown in Figure D3). This figure illustrates with direct numerical results the runoff generation process conceptually described by Thompson

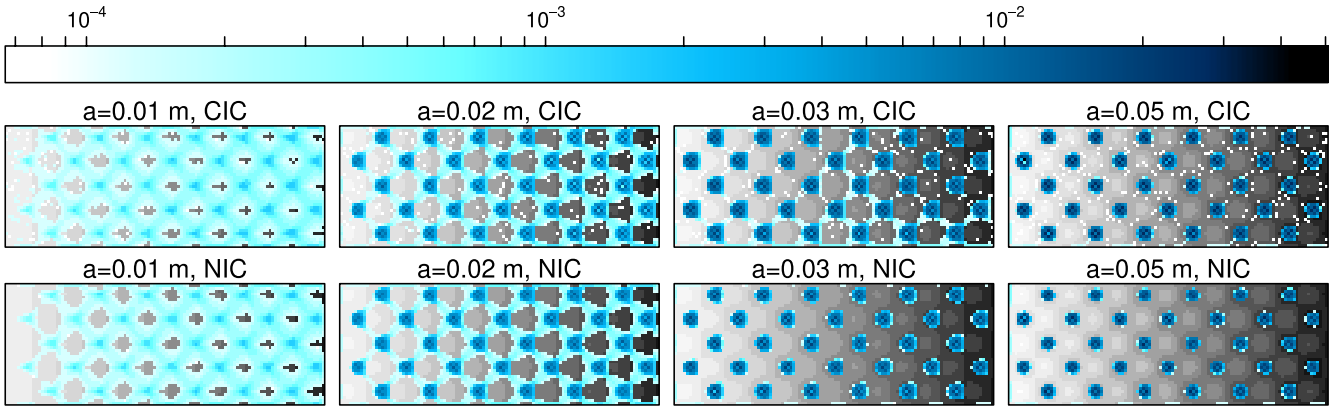

Figure 2. Water depth [m] distribution at the end of the rain $t = 1{,}800\ s$ (most flooded and connected state). Surfaces with $s = 0.05$, $\lambda = 1.2071$ m. Gray shades illustrate topography (darker is lower), blue colors represent water depth. Water depths lower than 0.1 mm are not shown. The surfaces slope to the right. Hydrographs for this case is shown in Figure 5.

et al. (2010) with regimes $\mathcal{A}$–$\mathcal{D}$, and Stage 1–3 of Darboux and Huang (2005) (Stage 1–3). At the start of the rain ($t \leq 600$s), Local Flow ($\mathcal{A}$)—Stage 1 runoff—occurs. During this time the surface is wet and water mostly flows into the depressions, progressively filling them. As the depressions are filled, water spills ($t = 660$s) from the upstream puddles into the downstream ones, that is , the so-called *fill-and-spill* or *puddle-to-puddle* (P2P) mechanisms (Chu, Yang et al., 2013; Darboux et al., 2002). Consequently, channels develop between flooded depressions ($t = 720$s), establishing Channel Flow ($\mathcal{B}$)—Stage 2 runoff—characterized by a rather 1D flow between puddles. This gradually transitions into Mixed Flow ($\mathcal{C}$), a regime with complex two-dimensional flow (Roche et al., 2007) in which some MT still protrudes above the water, as seen at $t \geq 780$s. Finally, full Sheet Flow ($\mathcal{D}$)—Stage 3 runoff—occurs, with the water covering the surface and inundating the MT entirely, but this is not achieved in the case shown in Figure 1 because rainfall was insufficient. This process is similar for all the simulated surfaces, albeit some regimes do not appear in some, depending on the slope and MT.

Figure 2 shows the water depth field for selected cases at $t = 1{,}800\ s$, just before the rain stops, that is, the most wet and most connected flow field. For some cases this also represents a (nearly) steady state flow. The depth distributions for $a = 0.01$ m (for both CIC and NIC) show a *mixed flow* ($\mathcal{C}$) regime, with CIC closer to a sheet flow ($\mathcal{D}$) regime. The depth distributions for $a = 0.02$ m show what may be considered a very developed form of *connected channel flow* ($\mathcal{B}$). This is clearly the case on the upstream end of the hillslope (left side of the domain), but the downstream end can be classified as a *mixed flow* ($\mathcal{C}$). That is, the regime varies spatially. Notably, the flow is somewhat less connected for the NIC than the CIC case. The depth distributions for $a = 0.03$ m show flow regimes of type $\mathcal{B}$ for CIC, and $\mathcal{A}$ for NIC. Finally, for the rougher $a = 0.05$ m case, both CIC and NIC clearly result in local flow $\mathcal{A}$.

Spatial distributions of accumulated infiltration show how MT affects partitioning into infiltration and runoff, in a time-integrated, yet spatially distributed way (Rossi & Ares, 2016). Figure 3 shows locally accumulated infiltration normalized by total infiltration in each cell F_i^* defined in Equation 8 at the end of the simulations ($t = 8000$s) for the same set of cases shown in Figure 2. There is a clear correlation between the spatial distributions of water depth and the accumulated infiltration. Poorly connected flow, such as the local flows ($\mathcal{A}$) result in rather binary infiltration distributions, with very low infiltration outside of the depressions, and very high infiltration in the depressions. This is particularly clear for $a = 0.05$ m, which also shows that, although the water depth distributions (Figure 2) are very similar for both the CIC and NIC, the accumulated infiltration is less heterogeneous for NIC than for CIC. That is, NIC slightly homogenizes infiltration in space, by allowing higher infiltration outside of depressions, and reducing infiltration in the depressions. Clearly, smoother surfaces with higher connectivity (mixed flows $\mathcal{C}$), result in accumulated infiltration distributions that are more homogeneous, and even more so for NIC, as clearly seen for the $a = 0.01$ m cases. For regimes with connected channelized flow ($\mathcal{B}$), the accumulated infiltration is more complex than the water depth distributions. For $a = 0.03$ m, the infiltration under NIC shows some subtle

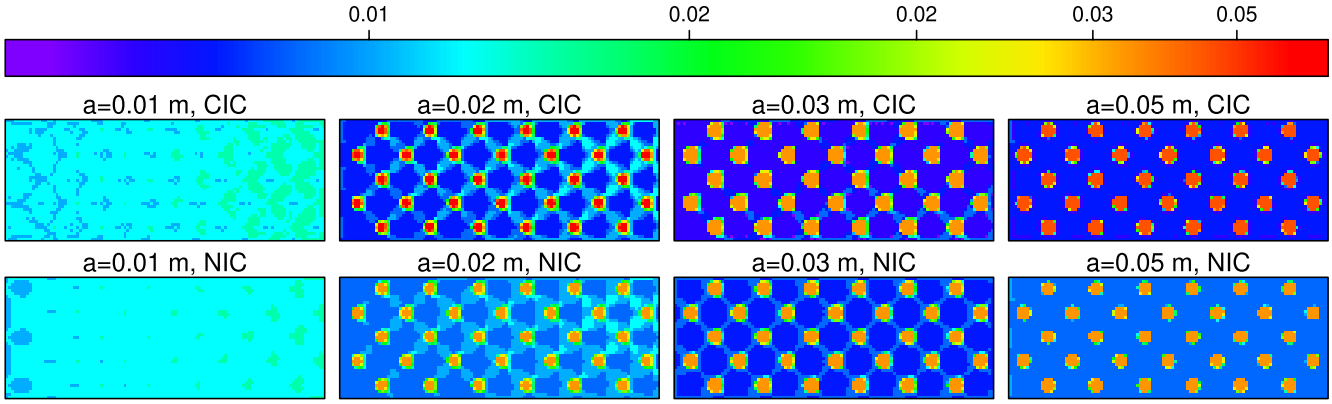

Figure 3. Local accumulated infiltration fraction $F^*(x, y)$ [%] at the end of the simulation (t = 8,000s). Surfaces with $s = 0.05$, $\lambda = 1.2071$ m. Water depths lower than 0.1 mm are not shown. The surfaces slope to the right. Non-constant infiltration capacity results in slightly more homogeneous distributions.

connectivity, albeit with extremely low water depths. NIC is again leads to more homogeneous infiltration patterns than CIC.

Figure 4 shows selected transient states of the accumulated infiltration $F(x, y)$ distribution. During the rain there is homogeneous infiltration. However, as soon as the rain stops, the drainage of the surface follows an inverse successions of the regimes, from $\mathcal{C}$ to $\mathcal{B}$ to $\mathcal{A}$, that is much faster than the filling process. The result is a drainage pattern that allows for longer infiltration times (and volumes), in the channels between puddles compared to the high points of MT 4. For the NIC counterpart (see Figure D4) the processes are similar, but the resulting patterns are somewhat different, even though the transient depth patterns are very similar between CIC and NIC. That is, there is an influence of the temporal variation of infiltration capacity on the spatial distribution of accumulated infiltration. This shows how accumulated infiltration may help reveal surface connectivity (Frei & Fleckenstein, 2014; Frei et al., 2010), and that heterogeneity arises in response once rain stops (Habtezion et al., 2016).

3.2. Macroscopic Signatures: Hydrographs

There are three characteristic hydrographs (Figure 5). The first type of hydrograph is henceforth called *full flow*—type FF—and is associated to the classic hydrographs resulting from runoff on a smooth plane under a steady pulse of rain, with a clear steady discharge plateau until the end of the rain (t = 1,800 s). The reference smooth surfaces, under CIC, result in FF hydrographs. Additionally, some MT surfaces also result in FF hydrographs (Figure 5), such as $a = \{0.01$ m, 0.02 m$\}$ under CIC. The steady state plateau of these

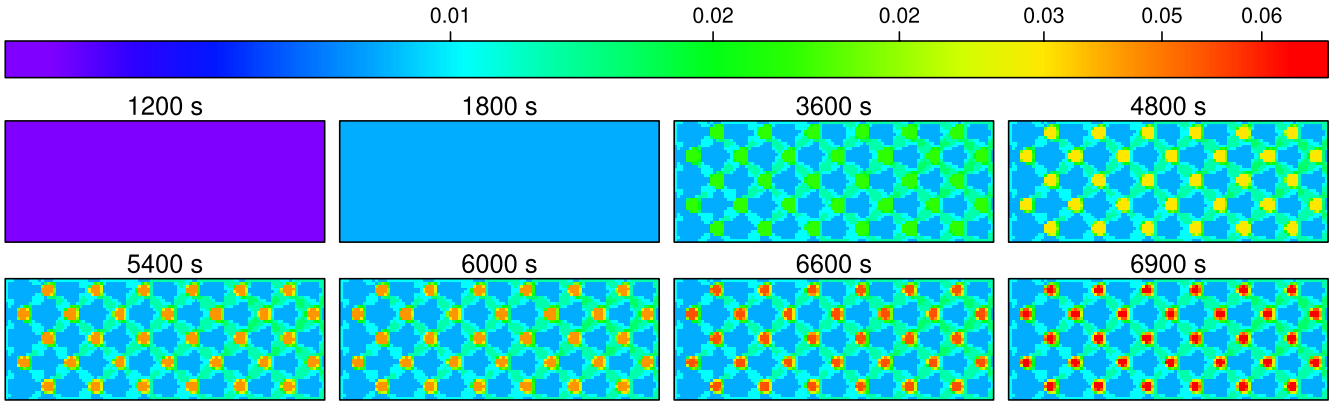

Figure 4. Accumulated infiltration [m] patterns, for different transient states. Surface with $s = 0.05$, $\lambda = 1.2071$ m and $a = 0.02$ m, and constant infiltration capacity. The surfaces slope to the right. Rainfall stops at t = 1,800s. The case is the same as Figure 1, but for different times. Infiltration heterogeneity develops after the rain.

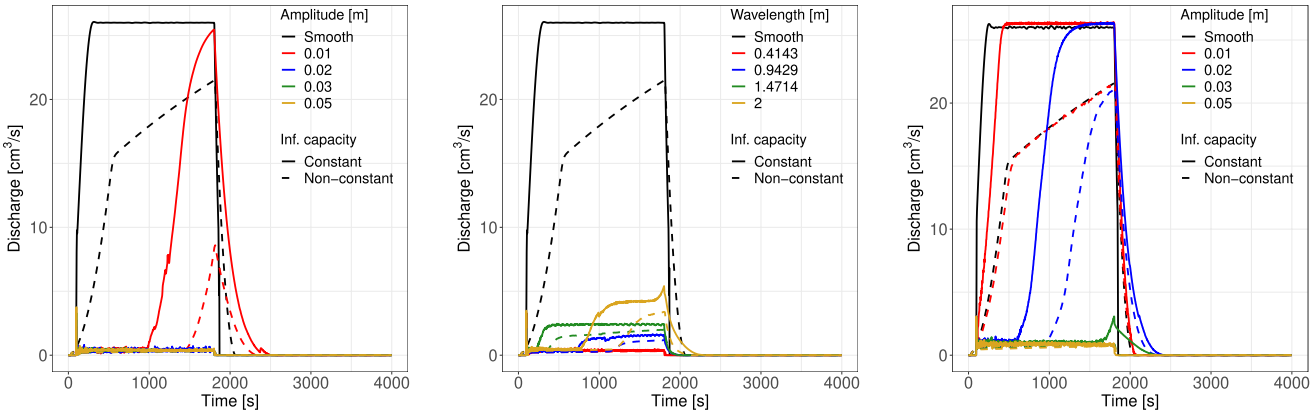

Figure 5. Hydrographs for selected surfaces, amplitude and wavelengths for both infiltration capacities, illustrating the different type of hydrograph shapes.

hydrographs is related to the establishment of a connected runoff field, that is , a large fraction of the surface is connected and drains to the outlet, and this fraction does not change during the event. FF hydrographs are the result of well connected surface flow, usually of mixed flow ($\mathcal{C}$) regimes and sometimes full sheet flow ($\mathcal{D}$) (Figure 2).

For NIC, the smooth reference case, and also MT cases $a = \{0.01\text{ m}, 0.02\text{ m}\}$ also result in FF but with a different hydrograph shape. The CIC FF hydrographs have three clear phases: a rising limb, a steady plateau, and a drainage limb. The rising and drainage limbs are also clearly in the NIC hydrographs. However, instead of the steady plateau, a second rising limb occurs. The steady plateau is caused by a steady flooded and connected flow area. For CIC, the infiltration capacity is also constant and steady flow can occur. For NIC, the infiltration capacity decreases over time, except when infiltration capacity has asymptotically reached the saturated conductivity (steady infiltration). Therefore, steady outflow cannot occur, even if the entire surface contributes. These are precisely the conditions of the second stage of the NIC FF hydrographs, that is , the surface contributing to runoff does not change, but infiltration capacity does (Figure 6a). This is

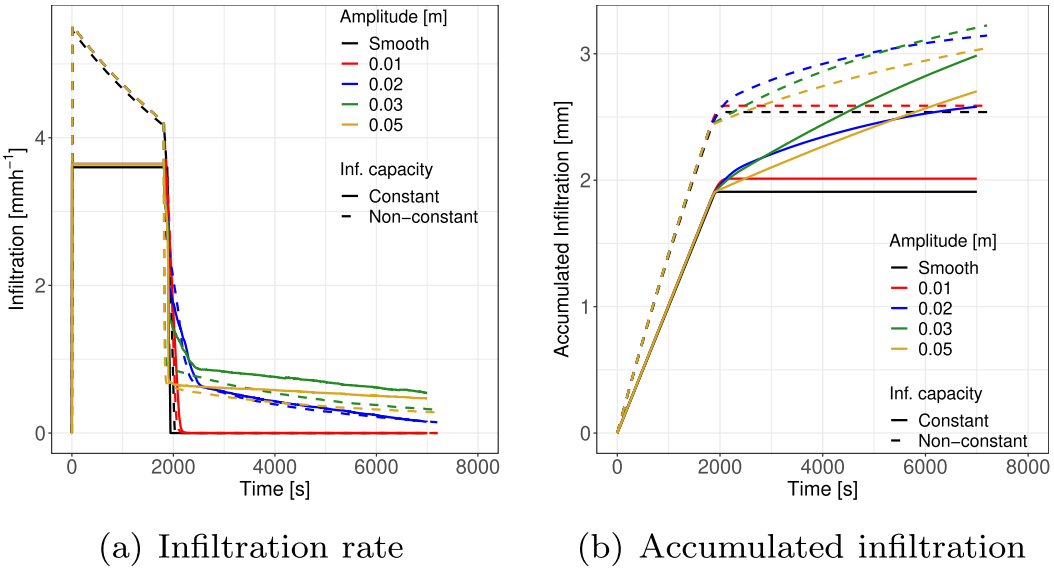

Figure 6. Time series of infiltration for selected cases $s = 0.05$, $\lambda = 0.1.2071$ m.

clearly seen for the $a = 0.01$ m case, for which both NIC and CIC produce very similar connected contributing runoff areas (Figure 2), but for which NIC does not result in a steady flow stage (Figure 5c).

The second type of hydrograph is the *connected flow*—type–CF—and is well illustrated by the $a = 0.01$ m CIC case in Figure 5a, and also by the NIC $a = 0.02$ m case in Figure 5c. Type CF shows a rising limb and a drainage limb, and only achieves a peak instead of a (nearly) steady stage. For hydrographs such as the CIC $a = 0.02$ m it remains unclear if they are of type CF or FF. For this surface, the flow is at the transition between channel and mixed flow ($\mathcal{B}$–$\mathcal{C}$), as seen in Figure 2. It is nonetheless clear that the channel flow regime $\mathcal{B}$ produces hydrographs of type CF which are the result of flows in which there is *puddle-to-puddle* connectivity, but not a fully developed 2D flow. CF hydrographs also have a rising limb does not start near the start of the rain $t = 0$s, but is lagged. For example, for both the CIC $a = 0.01$ m hydrograph in Figure 5a and the NIC $a = 0.02$ m in Figure 5c the rising limbs start at $t \approx 1{,}000$s. Prior to that there is a nearly steady non-zero discharge plateau, resulting from a small contributing area to the outlet. This stepped response, with an initial plateau can be explained by the transient depth distributions. Consider the case $a = 0.02$ m, CIC, which has a discharge plateau until $t \approx 600$s (Figure 5c). Figure 1 shows the transient depth distribution and that the puddles continue to progressively fill under a local flow $\mathcal{A}$ regime until $t = 6{,}000$s (equivalent NIC figure is available as Supporting Information, with similar behavior). The discharge is therefore the result of a very thin ($h \lesssim 0.1$ mm) water layers which flows from puddle to puddle, but still rather discontinuously. From $t = 660$s, a channel $\mathcal{B}$ regime occurs, in which there is clear transfer of water among depressions—*spill-and-fill* dynamics—which result in the onset of connected runoff, that is , the start of the rising limb of the hydrograph. By $t = 720$s this is well established and is only strengthened in time. It is interesting to note that, because all depressions are identical, they all filled almost simultaneously, therefore there is no clear cascade effect with multiple steps in the hydrographs, as has been reported for more realistic and variable MT (Appels et al., 2016; Darboux et al., 2002).

The last hydrograph type is the *boundary flow*—BF–type, such as the hydrographs for $a >= 0.03\ m$ in Figure 5a, with very little discharge. Other examples, in Figure 5b, are the cases with $\lambda \leq 1.471$. Hydrographs of type BF are the result of runoff being generated only near the boundary: only very local areas are contributing to the outlet, while the rest of the surface water remains disconnected. The only notable exception in shape of this hydrographs is the CIC $a = 0.03$ m case which shows an incipient peak exactly at the end of the rain, and could be classified as a CF hydrograph. Invoking the depth distributions of Figure 2, it is clear that both the $a = 0.05$ m, and the NIC $a = 0.03$ m cases with local flow $\mathcal{A}$ result in very clear BF hydrographs. The CIC $a = 0.03$ m case however, shows incipient channel flow $\mathcal{B}$, which explains the peaky behavior and why it results in a hydrograph between BF and CF. It is relevant to highlight that for the $a = 0.03$ m cases, changing the infiltration capacity from CIC to NIC affects both the regime and the hydrograph classification.

Figure 6 illustrates the domain-integrated infiltration rate Figure 6a and accumulated infiltration Figure 6b and highlights the different responses of CIC and NIC. Note that under the conditions simulated here, MT does not affect the net infiltration flux during rainfall because both infiltration models (CIC and NIC) are independent of water depth. Differences due to MT appear afterwards, as the puddles in each surface contain different water volumes that cannot run off and must therefore infiltrate. The accumulated infiltration shows very clearly how different MT results in different hydrological partitioning, as higher amplitudes (for the same slope and wavelength) tends to lead to more infiltration. Clearly, NIC results in higher infiltration than CIC.

In all cases, the runoff coefficient (c) is always $c < 0.5$, even for the reference smooth cases (see results for CIC in Supporting Information, Figure E5). This implies that the partitioning is weighted towards infiltration, which is why henceforth we favor studying infiltration metrics over runoff metrics. The runoff coefficients obtained here cannot be directly compared to real ones, as the idealized setup is quite simplistic in terms of the rainfall signal, and that the runoff coefficients is often the result of runoff integrated at a larger spatial scale.

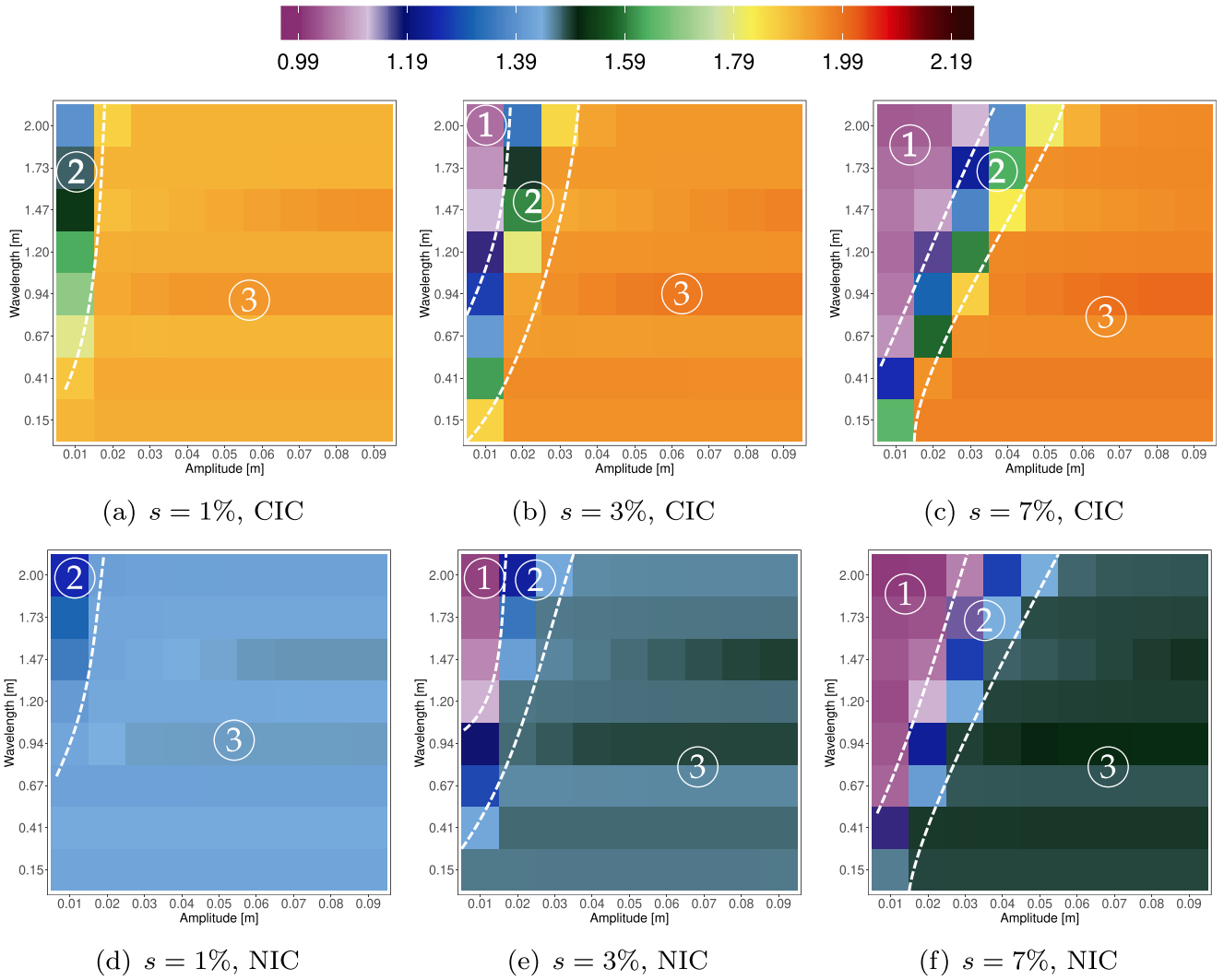

Figure 7. Infiltration enhancement $\tilde{I}$ [-] as a function of amplitude and wavelength, for different slopes and (top) constant (CIC) and (bottom) non-constant (NIC) infiltration. Color represents $\tilde{I}$, and sensitivity regions are iapproximately indicated.

3.3. Hydrological Balance & Infiltration Enhancement

Figure 7 shows selected results of the infiltration enhancement ratio $\tilde{I}$ for both constant (Figures 7a–7c) and time-varying (non constant; Figures 7d–7f) infiltration capacity. Each subfigure corresponds to one slope, and $\tilde{I}$ is shown as a function of amplitude and wavelength. There appear to be three regions, based on combinations of amplitude and wavelength (i.e., the $a - \lambda$ plane). Region ① corresponds to $\tilde{I}_c \approx 1$, that is, there is no infiltration enhancement due to MT, which means that MT has a very minor effect on the partitioning of rain into infiltration and runoff. This region tends to be absent for the mildest slopes. The other extreme is region ③, in which $\tilde{I} \to 2$ for CIC, and $\tilde{I} \to 1.5$ for NIC. In region ③ MT has a sizable effect on infiltration (and thus on the hydrological partitioning), but is not very sensitive to the particular features of MT, that is, amplitude and wavelength. In the intermediate region ②, $\tilde{I}$ is highly sensitive to the wavelength and amplitude, leading to a range of infiltration enhancement ratios. Moreover, the sensitivity of $\tilde{I}$ to the MT, and in which region of the $a - \lambda$ space the three regions fall, is a function of slope.

For $\tilde{I}_{cn}$, the three characteristic regions can also be identified in the $a - \lambda$ space (7). Region ① corresponds to $\tilde{I}_{cn} \approx 1$. In this region, the MT results in a very similar infiltration enhancement (compared to a smooth plane). That is, for MT in region ①, the response of the system is insensitive to the infiltration capacity

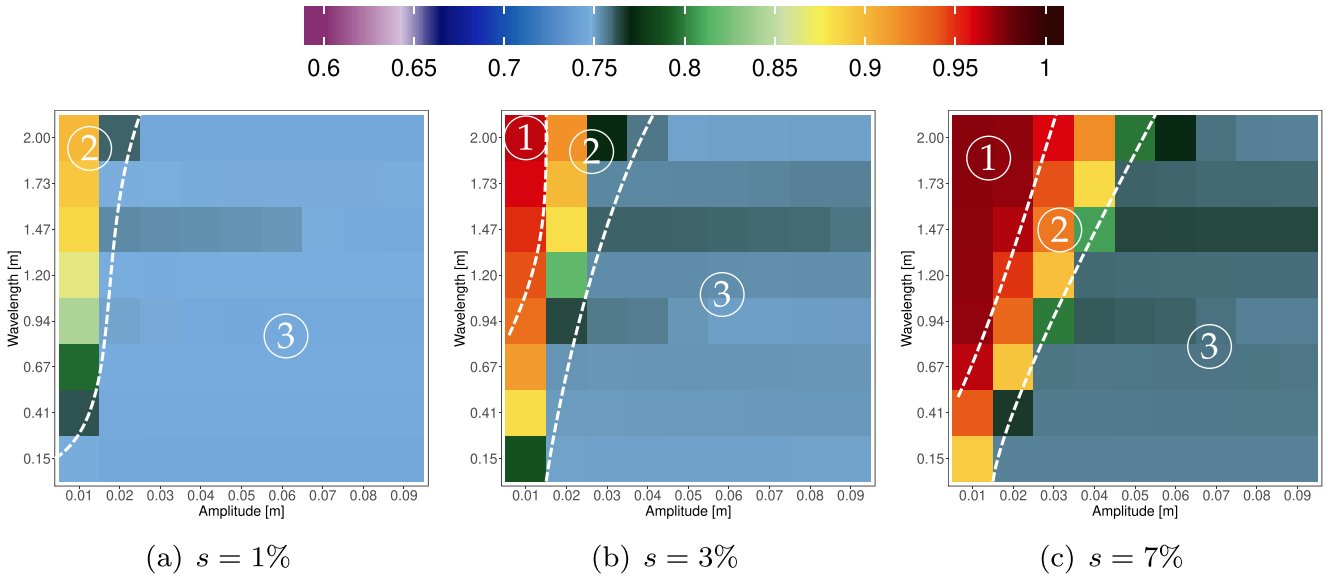

Figure 8. Infiltration enhancement ratio $\tilde{I}_{cn}$ [-] for selected slopes. The sensitivity regions are indicated approximately.

curve. The other two regions correspond roughly to $\tilde{I}_{cn} \lesssim 0.9$, meaning that MT has a smaller impact (infiltration enhancement) for NIC than CIC. Therefore, in this region, the hydrological partitioning is sensitive to both MT and infiltration capacity. Within this range of $\tilde{I}_{cn}$, it is possible to differentiate between two regions. Region ② is the high-sensitivity region in which values of $\tilde{I}_{cn}$ change rapidly with MT. Region ③, where $\tilde{I}_{cn} \to 0.75$, $\tilde{I}_{cn}$ (for the slopes in Figure 8, but $\tilde{I}_{cn} \to 0.65$ for all slopes) is insensitive to particular properties of the MT. Again, the position and size of these regions in the $a - \lambda$ plane is a function of slope, which is of course related to the behavior of $\tilde{I}$.

The three regions can also be identified for the ratio of infiltration volumes among NIC and CIC I_{cn} (Figure 9). Region ① corresponds to a rather constant $I_{cn} \approx 1.3$ in the $a - \lambda$ plane, implying that NIC results in a higher infiltration volume, but the infiltration volume is insensitive to MT. Region ② is, as before, quite sensitive to MT, but still leads to a higher infiltration volume for a non-constant infiltration capacity, that is,

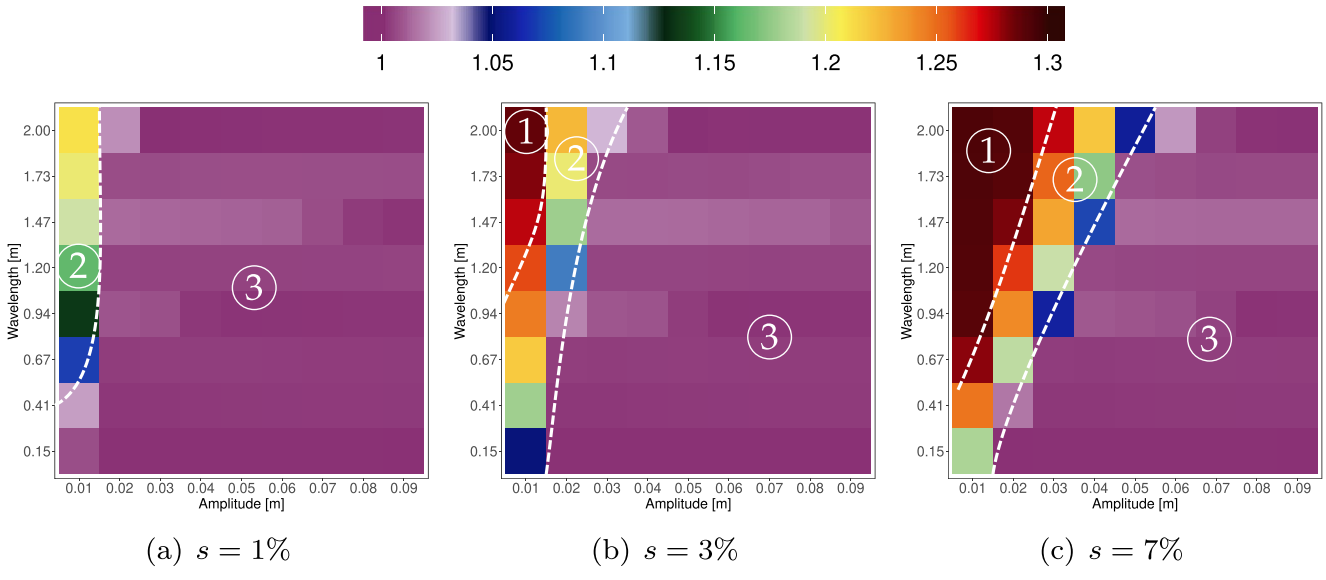

Figure 9. Infiltration volume ratio I_{cn} [-] for selected slopes. The sensitivity regions are indicated approximately.

Table 1
Summary of Regions, Indicators, Sensitivities, Hydrograph Classification and Regimes

Region	Indicators			Sensitivity to		Hydrograph	Developed flow regime
	$\tilde{I}$	$\tilde{I}_{cn}$	I_{cn}	MT	Inf. cap.		
①	≈1	≈1	≈1.3	–	+	FF	$\mathcal{D}$ / $\mathcal{C}$
②	1–2	0.65–1	1–1.3	++	++	CF	$\mathcal{B}$ / $\mathcal{C}$
③	→ 2	→ 0.65	≈1	+/−	+/−	BF	$\mathcal{A}$ / $\mathcal{B}$

FF: Full flow, CF: Connected flow, BF: Boundary Flow. $\mathcal{A}$: local flow, $\mathcal{B}$: channel flow, $\mathcal{C}$: mixed flow, $\mathcal{D}$: sheet flow.

$I_n > I_c$. Region ③, corresponding to $I_{cn} \approx 1$, meaning that $I_n \approx I_c$, that is , the infiltration volume is insensitive to both the infiltration capacity model and MT.

The conjunctive interpretation of the three indicators and the three regions is summarized in Table 1. In region ①, infiltration enhancement by MT is negligible for both infiltration capacity models, although more water infiltrates for NIC. This type of MT results in hydrological regimes that are insensitive to MT, but are sensitive to the infiltration capacity. In region ②, infiltration enhancement is strongly sensitive to the specific shapes of the MT, and somewhat higher under constant infiltration capacity. However, less water actually infiltrates with CIC. This MT type results in hydrological regimes that are strongly affected by both MT and the infiltration capacity model. Region ③ has the largest infiltration enhancements for both infiltration capacities. Although NIC reduces the effect of MT on infiltration enhancement, the enhancement itself remains insensitive to MT. Interestingly, the infiltration volume is not affected by the choice of infiltration capacity. This type of MT results in hydrological regimes that are insensitive to either the particular surface properties or to the infiltration capacity, but for which there is a large infiltration enhancement due to MT. It is noteworthy that for the lower slopes, there is no region ①. As slopes increase region ① appears and grows, whereas region ② is shifted towards higher amplitudes, and region ③ is displaced by region ②. This highlights the interactions between slope—a macroscale feature—and local MT—a small scale feature.

3.4. Microtopography Metrics and Infiltration Enhancement

MT amplitude and $\tilde{D}$ are strongly positively correlated (Thompson et al., 2010), and there is a weak negative relationship between $\tilde{D}$ and wavelength (see Supporting Information, Figure C1). The relationships between $\tilde{M}$ and amplitude/wavelength are trivial from Equation 10. Recall that $\tilde{D} \gg 1$ means that the depression volume is larger than the rainfall volume, and therefore runoff is unlikely to occur, even for impervious surfaces. For $\tilde{D} \ll 1$ the opposite is true and runoff is likely to occur, unless the infiltration capacity is higher than the rainfall intensity. For $\tilde{D} \approx 1$, it is unclear whether infiltration/ponding or runoff are more likely. Nonetheless, because runoff coefficients are $c < 0.5$, it is expected that the threshold for runoff will be roughly at $\tilde{D} \lessapprox 0.5$.

Figure 10 illustrates the relation between the microtopography ratio $\tilde{M}$, the depression storage ratio $\tilde{D}$ and the infiltration enhancement $\tilde{I}$. Figure 10a shows the strongly non-linear relationship between $\tilde{M}$ and $\tilde{D}$, and—as expected—the shape of this dependency is a function of slope. This is an indicator of the multiscale interaction in the system. For the same local MT ($\tilde{M}$), steeper slopes (a meso-scale property) have less depression storage. The three infiltration enhancement regions are hinted also by Figure 10a, in the color depiction of $\tilde{I}$. Note that the $\tilde{I}$ regions are different for CIC and NIC, but occur roughly at the same $\tilde{D}$. The figure shows that (for the 5% slope), region ① occurs only for $\tilde{D} < 0.01$, and regime ③, for both CIC and NIC, requires $\tilde{D} \gtrapprox 0.4$. This is similar for the MT ratio $\tilde{M}$. As Figure 10c shows, regime ① occurs for the smoother surfaces, that is, $\tilde{M} \gtrapprox 100$, and regime ③ for the roughest surfaces with $\tilde{M} \lessapprox 50$. In other words, although infiltration enhancement is different for CIC and NIC, the range of MT resulting in one or another regime remains the same for both infiltration capacity models, but is slope dependent. The rather robust position of the $\tilde{D}$ and $\tilde{M}$ thresholds for the different regions suggest that both indicators can help identify the hydrological behavior of the system.

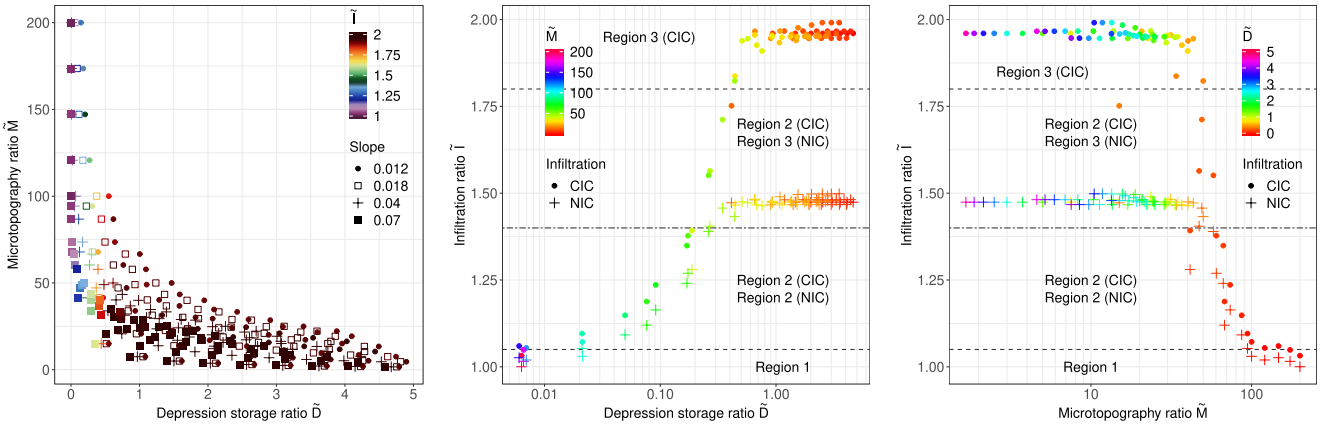

(a) $\tilde{D} - \tilde{M}$, CIC (b) $\tilde{I} - \tilde{D}$, $s = 0.05$ (c) $\tilde{I} - \tilde{M}$, $s = 0.05$

Figure 10. Relationships between geometry ratios $\tilde{M}$, $\tilde{D}$ and infiltration ratio $\tilde{I}$. Note the logarithmic transformations. The regions are marked in Figure 10b by dashed lines because there is no clear threshold.

Note however, that $\tilde{M}$ is strictly a local, structural property of the surface, whereas $\tilde{D}$ includes the slope, and also the rainfall volume.

4. Discussion

The results presented above, and the main insights summarized in Table 1 are consistent with previous results that have highlighted the strong role of MT on hydrological partitioning (Thompson et al., 2010), puddle-to-puddle connectivity onto smooth or stepped hydrographs (Appels et al., 2016; Darboux et al., 2002) and with the few reported spatiotemporal distributions of MT inundation (Yang & Chu, 2015). Nonetheless, our 2D results allows further insights and discussion beyond these previous insights. First, channel-flow ($\mathcal{B}$) and mixed-flow ($\mathcal{C}$) regimes can be observed, in contrast to the work of Thompson et al. (2010). This is particularly relevant, as our results suggest that such regimes correspond to the highest-sensitivity regions of runoff to MT. Our study points out that among the complex interactions of ponding, infiltration and runoff processes during rainfall events, MT may be dominant under some conditions, whereas infiltration capacity (and thus, soil properties and antecedent soil moisture) are more relevant in others. Additionally, the use of a spatially explicit and physically based model allows to relax many commonly used assumptions to study runoff generation over microtopographies, such as imperviousness (Antoine et al., 2009), or simplifications for *puddle-to-puddle* cellular-automata models (Chu, Yang et al., 2013; Yang & Chu, 2015). These results should not be naïvely transferred to specific hydrological systems, but rather provide a somewhat general framework to understand the effects of MT on runoff generation. The main caveat is that the MT structure used here is idealized, and representative only of very particular conditions (Kishné et al., 2014; Valtera & Schaetzl, 2017). The large variety of MT surfaces and complex interactions with other processes (e.g., subsurface flow, evaporation, erosion) still requires further investigation. Nonetheless, the approach could be used to analyze different MT structures, ranging from random topographical noise, to self-similar fractal MT, and also real surfaces. The challenge then becomes how to construct meaningful indices which characterize MT and allow for interpretability of the hydrologic results as a function of such indices.

Previous studies have investigated interactions of hydrological processes in response to MT, in particular related to subsurface (Frei & Fleckenstein, 2014; Frei et al., 2010, 2012) and shallow groundwater Van der Ploeg et al. (2012). Clearly our results do not account for subsurface processes (beyond infiltration, which acts mostly as a sink). However, as the aforementioned studies note, the water surface redistribution results in variability of infiltration, thus producing a strong control of subsurface dynamics. Overall, MT enhances infiltration, thus favoring soil and even groundwater recharge. Mata-González et al. (2012) noted that groundwater depths and MT were not correlated in a field study in California, but that local micro-environments were created for vegetation. Frei et al. (2012) also noted that MT can induce in/ex-filtration

cycles, which significantly affects local subsurface dynamics and may have strong implications on the biogeochemistry (Frei & Fleckenstein, 2014; Frei et al., 2012; Van der Ploeg et al., 2012). MT can, through water redistribution, affect vegetation establishment (McGrath et al., 2012) and species richness (Van der Ploeg et al., 2012). In return, vegetation and ecological dynamics, through different feedbacks, affect the formation and stability of MT (Saco & de las Heras, 2013; Rossi & Ares, 2017). The approach used here could be used as a base for virtual experiments on such feedbacks. Importantly, the strongest sensitivities observed here are not for highly connected sheet flow. This implies that different sensitivities to MT are expected to rainfall events with different intensities and volumes (Martin et al., 2008), as well as different sequences of rain (Van der Ploeg et al., 2012). Moreover, for large rainfall events (high volume and intensity), MT is likely to be less relevant than for small events. The latter favor less connected runoff, especially under intermittent rainfall, favoring a downhill cascade for transport of water and organic matter, nutrients and sediment which prompts a hierarchy of ecological responses (Austin et al., 2004; Schwinning & Sala, 2004).

4.1. Microtopography Indices

Maximum depression storage has been noted to be a poor predictor of hydrological behavior (Peñuela et al., 2015), since the actual storage in depressions is not passive or static, but dynamic and therefore dependent on rainfall and the interaction with infiltration (Rossi & Ares, 2012). However, the index $\tilde{D}$ used here seems to be a more robust indicator, as it is scaled by the rainfall volume. Furthermore, the distribution of $\tilde{D}$ values is highly non-linear. Regions ② and ③ are hard to differentiate linearly (see the linear color scale for $\tilde{D}$ in Figure 10c). In contrast, $\tilde{M}$ may be easier to interpret in a linear fashion (Figure 10b). Consequently, $\tilde{M}$ may be a more suitable indicator than $\tilde{D}$ to identify the regions hydrologically sensitive to MT (i.e., region ②).

4.2. Implications for Modeling

The results do have some practical implications from the point-of-view of spatially explicit modeling. In lumped models capturing MT is often done by using depression storage to capture the dominant effects of *spill-and-fill* processes (Amoah et al., 2012; Darboux et al., 2002; Grimm & Chu, 2019; Nasab et al., 2017), whereas in distributed models the question of spatial resolution is key, both for the DEM which may be unable to capture MT (Habtezion et al., 2016; Martin et al., 2008; Thomas et al., 2017; Zhao et al., 2020) and for mesh resolution (Caviedes-Voullième et al., 2012; Khosh Bin Ghomash et al., 2019; Özgen, Teuber et al., 2015). Explicitly representing MT can become computationally prohibitive (Frei & Fleckenstein, 2014; Frei et al., 2010), although current and foreseeable High-Performance Computing techniques (e.g., Le & Kumar, 2017; Morales-Hernández et al., 2020) and multiresolution modeling (Caviedes-Voullième, Gerhard et al., 2020; Özgen-Xian et al., 2020) are progressively making it feasible for catchment-scale systems. However, computational capacity is finite, which together with an inherently multiscale problem (Habtezion et al., 2016; Van der Ploeg et al., 2012; Voter & Loheide, 2018; Wu et al., 2020) makes the issue of resolution and scale inescapable. Below some spatial scale, MT and its effects (partitioning and connectivity) must be modeled in some *subgrid* fashion. The results here suggest that, for certain slopes and microtopographic features (region ①) it is possible to achieve accurate modeling results while strongly simplifying MT perhaps by using roughness formulations (Hughes et al., 2011; Özgen, Teuber et al., 2015), as its effects are almost negligible. Under the conditions of region ③, it may be possible to lump and parameterize MT into ponding, conveyance and infiltration models (Aksoy et al., 2016; Chu, Yang et al., 2013; Jan et al., 2018; Özgen, Liang et al., 2015; Shaw et al., 2012; Viero & Valipour, 2017; Yang & Chu, 2015). For region ②, the features and the specific geometry may need to be resolved, or at best, very accurately modeled. Inaccurately capturing MT has the risk of underestimating infiltration and overestimating runoff (e.g., Nasab et al., 2017) if standard soil parameters are used. Similarly, when calibrating infiltration parameters from runoff observations, there is the risk of over-fitting them, since ponded (and later perhaps evaporated) and infiltration volumes may be lumped (e.g., Fernández-Pato et al., 2016), further altering hydrological budgets (Le & Kumar, 2014). This has indeed been identified as a relevant issue in physically based hydrodynamic simulations in hydrology (e.g., Jan et al., 2018; Martin et al., 2008; Paniconi & Putti, 2015; Sande & Chu, 2012).

4.3. Limitations

A limitation of this study is the idealized sinusoidal MT, which is fundamentally isotropic, periodic and has a practically uniform distribution of surface roughness. Assessing the effects of irregular, more random and more realistic MT (e.g., Antoine et al., 2009; Appels et al., 2011; Peñuela et al., 2015) is necessary, since the shape of the probability density function of heights, spatial distribution, and its relation to depression storage (Kamphorst et al., 2005), MT anisotropy (Smith, 2014) and its variation along the hillslope (Wu et al., 2020) all affect runoff hydrodynamics. Moving into realistic surfaces clearly has the drawbacks of lower interpretability and requires more complex statistical indxicators to describe the surface MT, which is potentially not straightforward (Smith, 2014).

There are additional drivers of complexity and possible relevant interactions not explored in this numerical study, such as the heterogeneous soil infiltration capacity, antecedent storage (surface and subsurface) conditions, and temporal variability of rainfall. The possible combinations are endless, and beyond the scope of this paper. However, because of the relevance of such processes, we briefly discuss them here. It is likely that some level of structure exists between MT and heterogeneity of infiltration capacity due to small scale morphological and pedological processes (Rossi & Ares, 2017), that are intertwined with vegetation. For certain systems, MT depressions can be less pervious than the average surrounding soil, for example, due to deposition of fine material and crust formation (Pelletier et al., 2012), which may skew the hydrological balance towards evaporation, rather than infiltration. In systems with increased hydraulic conductivity in puddles, for example, due to higher soil moisture, the effect of MT will be further enhanced. Our use of Horton's infiltration capacity and a constant infiltration capacity mimics the response of an initially dry system that is wetted (thus reducing infiltration capacity) against one that can be thought of as initially wet (and thus with asymptotic or constant infiltration capacity). Our results therefore suggest that initially drier systems are somewhat less sensitive to MT than wetter systems. However, this cannot be simply generalized, as it would require an analysis of different infiltration capacity curves, and different rainfall signals. Rainfall variability, together with the shape of infiltration capacity curves, may substantially change the dynamics. In particular, rainfall variability will trigger a more complex response, leading to the transition from disconnected to connected flow during the onset of runoff, and vice-versa during the drainage phase, will happen multiple times during the event.

Additionally, both infiltration capacity representations used here are depth-independent, thus neglecting the pressure dependence of the infiltration fluxes. Thompson et al. (2011) argued that depth-independent infiltration representation may make the dynamics somewhat more transient (in comparison to depth-dependent) and give too much relevance to rainfall intensity in comparison to other hydraulic factors. Fernández-Pato et al. (2016) compared the results obtained with Horton and Green-Ampt equations on an 1D MT domain similar to Thompson et al. (2010). The Green-Ampt equation has some level of depth-dependency. They found that the difference in accumulated infiltration between Horton and Green-Ampt was less than 1%, and appeared mostly in the puddles. Furthermore, Fernández-Pato et al. (2018) tested a depth-dependent fractional order Green-Ampt formulation on hillslopes and first-order catchments showing improved predictability of rainfall-infiltration-runoff processes, but without fully resolving parametrization issues. Based on this, we argue that the effects of more sophisticated depth-dependent infiltration methods (e.g., Green-Ampt, or even Richards equation) may yield some small quantitative differences, but will lead to similar conclusions. We did not intend to represent any soil in particular, but only phenomenological represent near-dry (with a time-varying capacity) and wet soil infiltration capacity. The depth-dependency may yield somewhat different accumulated infiltration patterns as in Fernández-Pato et al. (2016), but seems non-critical for the overall behavior and consequent conclusions. Consequently, we kept the infiltration parametrization as simple as possible to focus and facilitate the investigation of the interactions.

4.4. Outlook

The study prompts an outlook into further exploring the interactions of more realistic MT structures with heterogeneous infiltration properties and realistic time-dependent rainfall signals. Additionally, understanding how the effects of MT may propagate across scales into larger systems remains to be explored. A systematic and formal link between MT, spatial distributions and the resulting hillslope scale signatures—

for example, hydrographs, hydrological partitioning, etc—is most likely best achieved through functional connectivity (Antoine et al., 2009; Appels et al., 2011; Mayor et al., 2008; Peñuela et al., 2015, 2016) and percolation metrics (Antoine et al., 2009; Lehmann et al., 2007). Such types of analysis may allow to tackle some of the interesting questions which remain to be addressed: how are hydrological dynamics modulated and smoothed out as the spatial scale of interest is increased? (Cammeraat, 2002; Cerdan et al., 2004; Dunne et al., 1991; Pavlovskii et al., 2019; Peñuela et al., 2015; Ries et al., 2017), which constitutes a clear next step following this work.

5. Summary and Conclusions

This numerical study on the effects of MT on rainfall partitioning and hydrograph characteristics study allows for a set of clear insights. (a) MT can have a wide range of effects on runoff generation and hydrological partitioning. Some of these effects can be very strong, such as significantly enhancing (up to doubling) infiltration volumes compared to a smooth planar hillslope with the same slope and rainfall. (b) Three categories of infiltration enhancement were identified, which correspond to three hydrodynamic regimes observed in hydrographs and spatiotemporal variations in surface flow. There is a set of MT properties ①, in which the MT has little effects, a set ② in which hydrological partitioning is very sensitive to MT, and a set ③ in which MT strongly favors infiltration, but insensitively to the specific MT properties. These sets define regions in the amplitude-wavelength space. (c) The identified regions generate particular flow regimes. Region ① corresponds to sheet flow regimes similar to flow over a smooth plane. Region ② is the result of connected, puddle-to-puddle flow. Region ③ corresponds to a strongly disconnected, local flow into the puddles. (d) Different infiltration capacity curves interact with the regions. Region ① is mostly affected by the rate of change of infiltration capacity over time. In region ② both MT and the shape of the infiltration capacity curve can strongly affect infiltration and runoff. Finally, in Region ③, surface slope plays the strongest role. Therefore, surfaces falling into regions ① and ③ are arguably dominated by the large scale surface features (slope), whereas responses in region ② are dominated by MT features. That is, rainfall-runoff problems are multiscale and the weight may shift from the small to the large scales depending on particular conditions. (e) Which combination of MT properties (in our case, amplitude and wavelength values) lead to which region is a function of slope, again highlighting the multiscale interactions. (f) A time varying infiltration capacity tends to homogenize the infiltration spatial distributions. The spatial infiltration heterogeneity occurs mostly after the rain.

Data Availability Statement

No data was used in this study, and all parameters required for model reproducibility are reported.

Acknowledgments
The authors are grateful to Ms. Andrea Domin for contributing in the preliminary exploration leading to this work. We also thank the Editor and anonymous reviewers for the constructive comments which have improved this manuscript.

References

Addor, N., Nearing, G., Prieto, C., Newman, A. J., Vine, N. L., & Clark, M. P. (2018). A ranking of hydrological signatures based on their predictability in space. *Water Resources Research*, *54*(11), 8792–8812. https://doi.org/10.1029/2018wr022606

Akan, A. O. (1992). Horton infiltration equation revisited. *Journal of Irrigation and Drainage Engineering*, *118*(5), 828–830. https://doi.org/10.1061/(asce)0733-9437(1992)118:5(828)

Aksoy, H., Gedikli, A., Unal, N. E., Yilmaz, M., Eris, E., Yoon, J., & Tayfur, G. (2016). Rainfall-runoff model considering microtopography simulated in a laboratory erosion flume. *Water Resources Management*, *30*(15), 5609–5624. https://doi.org/10.1007/s11269-016-1439-y

Amoah, J. K. O., Amatya, D. M., & Nnaji, S. (2012). Quantifying watershed surface depression storage: Determination and application in a hydrologic model. *Hydrological Processes*, *27*(17), 2401–2413. https://doi.org/10.1002/hyp.9364

Antoine, M., Javaux, M., & Bielders, C. (2009). What indicators can capture runoff-relevant connectivity properties of the micro-topography at the plot scale? *Advances in Water Resources*, *32*(8), 1297–1310. https://doi.org/10.1016/j.advwatres.2009.05.006

Antoine, M., Javaux, M., & Bielders, C. L. (2011). Integrating subgrid connectivity properties of the micro-topography in distributed runoff models, at the interrill scale. *Journal of Hydrology*, *403*(3–4), 213–223. https://doi.org/10.1016/j.jhydrol.2011.03.027

Appels, W. M., Bogaart, P. W., & van der Zee, S. E. (2011). Influence of spatial variations of microtopography and infiltration on surface runoff and field scale hydrological connectivity. *Advances in Water Resources*, *34*(2), 303–313. https://doi.org/10.1016/j.advwatres.2010.12.003

Appels, W. M., Bogaart, P. W., & van der Zee, S. E. (2016). Surface runoff in flat terrain: How field topography and runoff generating processes control hydrological connectivity. *Journal of Hydrology*, *534*, 493–504. https://doi.org/10.1016/j.jhydrol.2016.01.021

Austin, A. T., Yahdjian, L., Stark, J. M., Belnap, J., Porporato, A., Norton, U., et al. (2004). Water pulses and biogeochemical cycles in arid and semiarid ecosystems. *Oecologia*, *141*(2), 221–235. https://doi.org/10.1007/s00442-004-1519-1

Cammeraat, E. L. (2004). Scale dependent thresholds in hydrological and erosion response of a semi-arid catchment in southeast Spain. *Agriculture, Ecosystems & Environment*, *104*(2), 317–332. https://doi.org/10.1016/j.agee.2004.01.032

Cammeraat, L. H. (2002). A review of two strongly contrasting geomorphological systems within the context of scale. *Earth Surface Processes and Landforms*, *27*(11), 1201–1222. https://doi.org/10.1002/esp.421

Caviedes-Voullième, D., Fernández-Pato, J., & Hinz, C. (2018). Cellular automata and finite volume solvers converge for 2D shallow flow modelling for hydrological modelling. *Journal of Hydrology*, *563*, 411–417. https://doi.org/10.1016/j.jhydrol.2018.06.021

Caviedes-Voullième, D., Fernández-Pato, J., & Hinz, C. (2020). Performance assessment of 2D zero-inertia and shallow water models for simulating rainfall-runoff processes. *Journal of Hydrology*, *584*, 124663. https://doi.org/10.1016/j.jhydrol.2020.124663

Caviedes-Voullième, D., García-Navarro, P., & Murillo, J. (2012). Influence of mesh structure on 2D full shallow water equations and SCS Curve Number simulation of rainfall/runoff events. *Journal of Hydrology*, *448–449*, 39–59. https://doi.org/10.1016/j.jhydrol.2012.04.006

Caviedes-Voullième, D., Gerhard, N., Sikstel, A., & Müller, S. (2020). Multiwavelet-based mesh adaptivity with discontinuous galerkin schemes: Exploring 2D shallow water problems. *Advances in Water Resources*, *138*, 103559. https://doi.org/10.1016/j.advwatres.2020.103559

Cerdan, O., Bissonnais, Y. L., Govers, G., Lecomte, V., van Oost, K., Couturier, A., et al. (2004). Scale effect on runoff from experimental plots to catchments in agricultural areas in Normandy. *Journal of Hydrology*, *299*(1–2), 4–14. https://doi.org/10.1016/j.jhydrol.2004.02.017

Chu, X., Nelis, J., & Rediske, R. (2013). Preliminary study on the effects of surface microtopography on tracer transport in a coupled overland and unsaturated flow system. *Journal of Hydrologic Engineering*, *18*(10), 1241–1249. https://doi.org/10.1061/(asce)he.1943-5584.0000729

Chu, X., Yang, J., Chi, Y., & Zhang, J. (2013). Dynamic puddle delineation and modeling of puddle-to-puddle filling-spilling-merging-splitting overland flow processes. *Water Resources Research*, *49*(6), 3825–3829. https://doi.org/10.1002/wrcr.20286

Darboux, F., Davy, P., Gascuel-Odoux, C., & Huang, C. (2002). Evolution of soil surface roughness and flowpath connectivity in overland flow experiments. *CATENA*, *46*(2–3), 125–139. https://doi.org/10.1016/s0341-8162(01)00162-x

Darboux, F., & Huang, C.-H. (2005). Does soil surface roughness increase or decrease water and particle transfers? *Soil Science Society of America Journal*, *69*(3), 748–756. https://doi.org/10.2136/sssaj2003.0311

Descroix, L., Viramontes, D., Estrada, J., Barrios, J.-L. G., & Asseline, J. (2007). Investigating the spatial and temporal boundaries of hortonian and hewlettian runoff in northern Mexico. *Journal of Hydrology*, *346*(3–4), 144–158. https://doi.org/10.1016/j.jhydrol.2007.09.009

Dunne, T., Zhang, W., & Aubry, B. F. (1991). Effects of rainfall, vegetation, and microtopography on infiltration and runoff. *Water Resources Research*, *27*(9), 2271–2285. https://doi.org/10.1029/91wr01585

Fernández-Pato, J., Caviedes-Voullième, D., & García-Navarro, P. (2016). Rainfall/runoff simulation with 2D full shallow water equations: Sensitivity analysis and calibration of infiltration parameters. *Journal of Hydrology*, *536*, 496–513. https://doi.org/10.1016/j.jhydrol.2016.03.021

Fernández-Pato, J., Gracia, J. L., & García-Navarro, P. (2018). A fractional-order infiltration model to improve the simulation of rainfall/runoff in combination with a 2D shallow water model. *Journal of Hydroinformatics*, *20*(4), 898–916. https://doi.org/10.2166/hydro.2018.145

Frei, S., & Fleckenstein, J. (2014). Representing effects of micro-topography on runoff generation and sub-surface flow patterns by using superficial rill/depression storage height variations. *Environmental Modelling & Software*, *52*, 5–18. https://doi.org/10.1016/j.envsoft.2013.10.007

Frei, S., Knorr, K. H., Peiffer, S., & Fleckenstein, J. H. (2012). Surface micro-topography causes hot spots of biogeochemical activity in wetland systems: A virtual modeling experiment. *Journal of Geophysical Research*, *117*(G4), G00N12. https://doi.org/10.1029/2012jg002012

Frei, S., Lischeid, G., & Fleckenstein, J. (2010). Effects of micro-topography on surface-subsurface exchange and runoff generation in a virtual riparian wetland - A modeling study. *Advances in Water Resources*, *33*(11), 1388–1401. https://doi.org/10.1016/j.advwatres.2010.07.006

García-Serrana, M., Gulliver, J. S., & Nieber, J. L. (2018). Description of soil micro-topography and fractional wetted area under runoff using fractal dimensions. *Earth Surface Processes and Landforms*, *43*(13), 2685–2697. https://doi.org/10.1002/esp.4424

Grieve, S. W., Mudd, S. M., & Hurst, M. D. (2016). How long is a hillslope? *Earth Surface Processes and Landforms*, *41*(8), 1039–1054. https://doi.org/10.1002/esp.3884

Grimm, K., & Chu, X. (2019). Depression threshold control proxy to improve HEC-HMS modeling of depression-dominated watersheds. *Hydrological Sciences Journal*, *65*(2), 200–211. https://doi.org/10.1080/02626667.2019.1690148

Habtezion, N., Nasab, M. T., & Chu, X. (2016). How does DEM resolution affect microtopographic characteristics, hydrologic connectivity, and modelling of hydrologic processes? *Hydrological Processes*, *30*(25), 4870–4892. https://doi.org/10.1002/hyp.10967

Hansen, B., Schjønning, P., & Sibbesen, E. (1999). Roughness indices for estimation of depression storage capacity of tilled soil surfaces. *Soil and Tillage Research*, *52*(1–2), 103–111. https://doi.org/10.1016/s0167-1987(99)00061-6

Harman, C. J., Lohse, K. A., Troch, P. A., & Sivapalan, M. (2014). Spatial patterns of vegetation, soils, and microtopography from terrestrial laser scanning on two semiarid hillslopes of contrasting lithology. *Journal of Geophysical Research: Biogeosciences*, *119*(2), 163–180. https://doi.org/10.1002/2013JG002507

Helming, K., Römkens, M. J. M., & Prasad, S. N. (1998). Surface roughness related processes of runoff and soil loss: A flume study. *Soil Science Society of America Journal*, *62*(1), 243–250. https://doi.org/10.2136/sssaj1998.03615995006200010031x

Horton, R. E. (1933). The role of infiltration in the hydrologic cycle. *Transactions, American Geophysical Union*, *14*(1), 446. https://doi.org/10.1029/tr014i001p00446

Hu, L., Bao, W., Shi, P., Wang, J., & Lu, M. (2020). Simulation of overland flow considering the influence of topographic depressions. *Scientific Reports*, *10*(1). https://doi.org/10.1038/s41598-020-63001-y

Hughes, J., Decker, J., & Langevin, C. (2011). Use of upscaled elevation and surface roughness data in two-dimensional surface water models. *Advances in Water Resources*, *34*(9), 1151–1164. https://doi.org/10.1016/j.advwatres.2011.02.004

Jan, A., Coon, E. T., Graham, J. D., & Painter, S. L. (2018). A subgrid approach for modeling microtopography effects on overland flow. *Water Resources Research*, *54*(9), 6153–6167. https://doi.org/10.1029/2017wr021898

Kamphorst, E., Chadœuf, J., Jetten, V., & Guérif, J. (2005). Generating 3d soil surfaces from 2d height measurements to determine depression storage. *CATENA*, *62*(2–3), 189–205. https://doi.org/10.1016/j.catena.2005.05.006

Khitrov, N. B. (2016). Properties and regimes of vertisols with gilgai microtopography (a review). *Eurasian Soil Science*, *49*(3), 257–271. https://doi.org/10.1134/s1064229316030054

Khosh Bin Ghomash, S., Caviedes-Voullième, D., & Hinz, C. (2019). Effects of erosion-induced changes to topography on runoff dynamics. *Journal of Hydrology*, *573*, 811–828. https://doi.org/10.1016/j.jhydrol.2019.04.018

Kishné, A., Morgan, C., & Neely, H. (2014). How much surface water can gilgai microtopography capture? *Journal of Hydrology*, *513*, 256–261. https://doi.org/10.1016/j.jhydrol.2014.03.053

Langhans, C., Govers, G., Diels, J., Leys, A., Clymans, W., den Putte, A. V., & Valckx, J. (2011). Experimental rainfall–runoff data: Reconsidering the concept of infiltration capacity. *Journal of Hydrology*, *399*(3–4), 255–262. https://doi.org/10.1016/j.jhydrol.2011.01.005

Le, P. V. V., & Kumar, P. (2014). Power law scaling of topographic depressions and their hydrologic connectivity. *Geophysical Research Letters*, *41*(5), 1553–1559. https://doi.org/10.1002/2013gl059114
Le, P. V. V., & Kumar, P. (2017). Interaction between ecohydrologic dynamics and microtopographic variability under climate change. *Water Resources Research*, *53*(10), 8383–8403. https://doi.org/10.1002/2017WR020377
Lehmann, P., Hinz, C., McGrath, G., van Meerveld, H. J. T., & McDonnell, J. J. (2007). Rainfall threshold for hillslope outflow: An emergent property of flow pathway connectivity. *Hydrology and Earth System Sciences*, *11*(2), 1047–1063. https://doi.org/10.5194/hess-11-1047-2007
Llasat, M.-C. (2001). An objective classification of rainfall events on the basis of their convective features: Application to rainfall intensity in the northeast of Spain. *International Journal of Climatology*, *21*(11), 1385–1400. https://doi.org/10.1002/joc.692
Luo, J., Zheng, Z., Li, T., & He, S. (2017). Spatial heterogeneity of microtopography and its influence on the flow convergence of slopes under different rainfall patterns. *Journal of Hydrology*, *545*, 88–99. https://doi.org/10.1016/j.jhydrol.2016.12.018
Luo, J., Zheng, Z., Li, T., & He, S. (2020). Temporal variations in runoff and sediment yield associated with soil surface roughness under different rainfall patterns. *Geomorphology*, *349*, 106915. https://doi.org/10.1016/j.geomorph.2019.106915
Martin, Y., Valeo, C., & Tait, M. (2008). Centimetre-scale digital representations of terrain and impacts on depression storage and runoff. *CATENA*, *75*(2), 223–233. https://doi.org/10.1016/j.catena.2008.07.005
Mata-González, R., McLendon, T., Martin, D. W., Trlica, M. J., & Pearce, R. A. (2012). Vegetation as affected by groundwater depth and microtopography in a shallow aquifer area of the great basin. *Ecohydrology*, *5*(1), 54–63. https://doi.org/10.1002/eco.196
Mayor, Á. G., Bautista, S., Small, E. E., Dixon, M., & Bellot, J. (2008). Measurement of the connectivity of runoff source areas as determined by vegetation pattern and topography: A tool for assessing potential water and soil losses in drylands. *Water Resources Research*, *44*(10), W10423. https://doi.org/10.1029/2007WR006367
McClain, M. E., Boyer, E. W., Dent, C. L., Gergel, S. E., Grimm, N. B., Groffman, P. M., et al. (2003). Biogeochemical hot spots and hot moments at the interface of terrestrial and aquatic ecosystems. *Ecosystems*, *6*(4), 301–312. https://doi.org/10.1007/s10021-003-0161-9
McGrath, G. S., Paik, K., & Hinz, C. (2012). Microtopography alters self-organized vegetation patterns in water-limited ecosystems. *Journal of Geophysical Research*, *117*(G3), G03021. https://doi.org/10.1029/2011JG001870
McMillan, H., Westerberg, I., & Branger, F. (2017). Five guidelines for selecting hydrological signatures. *Hydrological Processes*, *31*(26), 4757–4761. https://doi.org/10.1002/hyp.11300
Mishra, S. K., Tyagi, J. V., & Singh, V. P. (2003). Comparison of infiltration models. *Hydrological Processes*, *17*(13), 2629–2652. https://doi.org/10.1002/hyp.1257
Morales-Hernández, M., Sharif, M. B., Gangrade, S., Dullo, T. T., Kao, S.-C., Kalyanapu, A., et al. (2020). High-performance computing in water resources hydrodynamics. *Journal of Hydroinformatics*, *22*, 1217–1235. https://doi.org/10.2166/hydro.2020.163
Müller, E. N., Wainwright, J., & Parsons, A. J. (2007). Impact of connectivity on the modeling of overland flow within semiarid shrubland environments. *Water Resources Research*, *43*(9), W09412. https://doi.org/10.1029/2006WR005006
Nasab, M. T., Singh, V., & Chu, X. (2017). SWAT modeling for depression-dominated areas: How do depressions manipulate hydrologic modeling? *Water*, *9*(1), 58. https://doi.org/10.3390/w9010058
Onstad, C. A. (1984). Depressional storage on tilled soil surfaces. *Transactions of the ASABE*, *27*(3), 729–732. https://doi.org/10.13031/2013.32861
Özgen, I., Liang, D., & Hinkelmann, R. (2015). Shallow water equations with depth-dependent anisotropic porosity for subgrid-scale topography. *Applied Mathematical Modelling*, *40*. https://doi.org/10.1016/j.apm.2015.12.012
Özgen, I., Teuber, K., Simons, F., Liang, D., & Hinkelmann, R. (2015). Upscaling the shallow water model with a novel roughness formulation. *Environmental Earth Sciences*, *74*(11), 7371–7386. https://doi.org/10.1007/s12665-015-4726-7
Özgen-Xian, I., Kesserwani, G., Caviedes-Voullième, D., Molins, S., Xu, Z., Dwivedi, D., et al. (2020). Wavelet-based local mesh refinement for rainfall–runoff simulations. *Journal of Hydroinformatics*, *22*, 1059–1077. https://doi.org/10.2166/hydro.2020.198
Paniconi, C., & Putti, M. (2015). Physically based modeling in catchment hydrology at 50: Survey and outlook. *Water Resources Research*, *51*(9), 7090–7129. https://doi.org/10.1002/2015WR017780
Pavlovskii, I., Noorduijn, S. L., Liggett, J. E., Klassen, J., & Hayashi, M. (2019). Quantifying terrain controls on runoff retention and routing in the northern prairies. *Hydrological Processes*, *34*, 473–484. https://doi.org/10.1002/hyp.13599
Pelletier, J. D., DeLong, S. B., Orem, C. A., Becerra, P., Compton, K., Gressett, K., & Spinler, J. C. (2012). How do vegetation bands form in dry lands? insights from numerical modeling and field studies in southern Nevada, USA. *Journal of Geophysical Research*, *117*(F4), F04026. https://doi.org/10.1029/2012JF002465
Peñuela, A., Darboux, F., Javaux, M., & Bielders, C. L. (2016). Evolution of overland flow connectivity in bare agricultural plots. *Earth Surface Processes and Landforms*, *41*(11), 1595–1613. https://doi.org/10.1002/esp.3938
Peñuela, A., Javaux, M., & Bielders, C. L. (2015). How do slope and surface roughness affect plot-scale overland flow connectivity? *Journal of Hydrology*, *528*, 192–205. https://doi.org/10.1016/j.jhydrol.2015.06.031
Ries, F., Schmidt, S., Sauter, M., & Lange, J. (2017). Controls on runoff generation along a steep climatic gradient in the Eastern Mediterranean. *Journal of Hydrology: Regional Studies*, *9*, 18–33. https://doi.org/10.1016/j.ejrh.2016.11.001
Roche, N., Daïan, J.-F., & Lawrence, D. S. L. (2007). Hydraulic modeling of runoff over a rough surface under partial inundation. *Water Resources Research*, *43*(8), W08410. https://doi.org/10.1029/2006WR005484
Rossi, M. J., & Ares, J. O. (2012). Depression storage and infiltration effects on overland flow depth-velocity-friction at desert conditions: Field plot results and model. *Hydrology and Earth System Sciences*, *16*(9), 3293–3307. https://doi.org/10.5194/hess-16-3293-2012
Rossi, M. J., & Ares, J. O. (2016). Overland flow from plant patches: Coupled effects of preferential infiltration, surface roughness and depression storage at the semiarid patagonian Monte. *Journal of Hydrology*, *533*, 603–614. https://doi.org/10.1016/j.jhydrol.2015.12.028
Rossi, M. J., & Ares, J. O. (2017). Water fluxes between inter-patches and vegetated mounds in flat semiarid landscapes. *Journal of Hydrology*, *546*, 219–229. https://doi.org/10.1016/j.jhydrol.2017.01.016
Saco, P. M., & de las Heras, M. M. (2013). Ecogeomorphic coevolution of semiarid hillslopes: Emergence of banded and striped vegetation patterns through interaction of biotic and abiotic processes. *Water Resources Research*, *49*(1), 115–126. https://doi.org/10.1029/2012WR012001
Sande, L., & Chu, X. (2012). Laboratory experiments on the effect of microtopography on soil-water movement: Spatial variability in wetting front movement. *Applied and Environmental Soil Science*, *2012*, 1–8. https://doi.org/10.1155/2012/679210
Schwinning, S., & Sala, O. E. (2004). Hierarchy of responses to resource pulses in arid and semi-arid ecosystems. *Oecologia*, *141*(2), 211–220. https://doi.org/10.1007/s00442-004-1520-8
Shaw, D. A., Pietroniro, A., & Martz, L. (2012). Topographic analysis for the prairie pothole region of western Canada. *Hydrological Processes*, *27*, 3105–3114. https://doi.org/10.1002/hyp.9409

Smith, M. W. (2014). Roughness in the Earth sciences. *Earth-Science Reviews*, *136*, 202–225. https://doi.org/10.1016/j.earscirev.2014.05.016

Tatard, L., Planchon, O., Wainwright, J., Nord, G., Favis-Mortlock, D., Silvera, N., et al. (2008). Measurement and modelling of high-resolution flow-velocity data under simulated rainfall on a low-slope sandy soil. *Journal of Hydrology*, *348*(1–2), 1–12. https://doi.org/10.1016/j.jhydrol.2007.07.016

Thomas, I., Jordan, P., Shine, O., Fenton, O., Mellander, P.-E., Dunlop, P., & Murphy, P. (2017). Defining optimal DEM resolutions and point densities for modelling hydrologically sensitive areas in agricultural catchments dominated by microtopography. *International Journal of Applied Earth Observation and Geoinformation*, *54*, 38–52. https://doi.org/10.1016/j.jag.2016.08.012

Thompson, S., Katul, G., Konings, A., & Ridolfi, L. (2011). Unsteady overland flow on flat surfaces induced by spatial permeability contrasts. *Advances in Water Resources*, *34*(8), 1049–1058. https://doi.org/10.1016/j.advwatres.2011.05.012

Thompson, S. E., Katul, G. G., & Porporato, A. (2010). Role of microtopography in rainfall-runoff partitioning: An analysis using idealized geometry. *Water Resources Research*, *46*(7), W07520. https://doi.org/10.1029/2009WR008835

Turunen, M., Turtola, E., Vaaja, M., Hyväluoma, J., & Koivusalo, H. (2020). Terrestrial laser scanning data combined with 3d hydrological modeling decipher the role of tillage in field water balance and runoff generation. *CATENA*, *187*, 104363. https://doi.org/10.1016/j.catena.2019.104363

Valtera, M., & Schaetzl, R. J. (2017). Pit-mound microrelief in forest soils: Review of implications for water retention and hydrologic modelling. *Forest Ecology and Management*, *393*, 40–51. https://doi.org/10.1016/j.foreco.2017.02.048

Van der Ploeg, M., Appels, W., Cirkel, D., Oosterwoud, M., Witte, J.-P., & van der Zee, S. (2012). Microtopography as a driving mechanism for ecohydrological processes in shallow groundwater systems. *Vadose Zone Journal*, *11*(3), vzj2011.0098. https://doi.org/10.2136/vzj2011.0098

Viero, D. P., & Valipour, M. (2017). Modeling anisotropy in free-surface overland and shallow inundation flows. *Advances in Water Resources*, *104*, 1–14. https://doi.org/10.1016/j.advwatres.2017.03.007

Voter, C. B., & Loheide, S. P. (2018). Urban residential surface and subsurface hydrology: Synergistic effects of low-impact features at the parcel scale. *Water Resources Research*, *54*(10), 8216–8233. https://doi.org/10.1029/2018wr022534

Wainwright, J., & Bracken, L. J. (2011). Runoff generation, overland flow and erosion on hillslopes. In Arid zone geomorphology (pp. 235–267). John Wiley & Sons, Ltd. https://doi.org/10.1002/9780470710777.ch11

Wu, S., Chen, L., Wang, N., Li, J., & Li, J. (2020). Two-dimensional rainfall-runoff and soil erosion model on an irregularly rilled hillslope. *Journal of Hydrology*, *580*, 124346. https://doi.org/10.1016/j.jhydrol.2019.124346

Yang, J., & Chu, X. (2013). Quantification of the spatio-temporal variations in hydrologic connectivity of small-scale topographic surfaces under various rainfall conditions. *Journal of Hydrology*, *505*, 65–77. https://doi.org/10.1016/j.jhydrol.2013.09.013

Yang, J., & Chu, X. (2015). A new modeling approach for simulating microtopography-dominated, discontinuous overland flow on infiltrating surfaces. *Advances in Water Resources*, *78*, 80–93. https://doi.org/10.1016/j.advwatres.2015.02.004

Zhao, L., Hou, R., & Wu, F. (2020). Effect of DEM grid size on microrelief indexes estimation for sloping lands after reservoir tillage. *Soil and Tillage Research*, *196*, 104451. https://doi.org/10.1016/j.still.2019.104451

Zhao, L., & Wu, F. (2015). Simulation of runoff hydrograph on soil surfaces with different microtopography using a travel time method at the plot scale. *PloS One*, *10*(6), e0130794. https://doi.org/10.1371/journal.pone.0130794

Zhao, W., & Liu, B. (2010). The response of sap flow in shrubs to rainfall pulses in the desert region of China. *Agricultural and Forest Meteorology*, *150*(9), 1297–1306. https://doi.org/10.1016/j.agrformet.2010.05.012